Upper Boundary Condition for Asteroseismological Modelling of Solar-type Stars

by

K. Christopher Cooke

A Thesis Submitted to
Saint Mary's University, Halifax, Nova Scotia
in Partial Fulfillment of the Requirements for
the Degree of Master of Science in Astronomy
(Department of Astronomy and Physics)

August 14, 2013, Halifax, Nova Scotia

Approved: Dr. Ian Short (Supervisor)

Approved: Dr. David Guenther (Supervisor)

Approved: Dr. David Turner (Examiner)

Date: November 28, 2013.

Acknowledgements

I would like to thank my supervisors, Drs. Ian Short and David Guenther, for all of their guidance and help over the past two years. I'd also like to express my gratitude to Dr. David Turner for taking the time to sit on my defence committee, and for correcting the landslide of grammatical errors that were originally contained within these pages.

I would also like to thank all of my friends and fellow graduate students in the Department of Astronomy and Physics. Liz, Sam, Mitch, Kirsten, Bobby, Anneya, Diego, Rasalhague, Jenn, Jaspreet, Esteban, Ghazaleh, Maan, Amit, Michael, Jason, Sherry, Dan, James, Dave, Chris, Shelly, and Jenice. You guys made it so that I always looked forward to coming in to school every day.

I couldn't have done this without the great support of my friends and family. My parents, grandparents, and aunts and uncles were always there for me to lend their support when times got tough. Nor can I forget the enrichments that Marie, Terra, Shawn, Duncan, Lucy, Jason, Agatha, Ferenc, Thomas, Danica, Henry, Matilda, Oliver, and Baylee have made to my life over the years. And, of course, Robyn, whose love and support through this project will never, ever be forgotten.

Finally, I would like to acknowledge NSERC and FGSR for their financial support for this research, and ACEnet for the use of their computational resources.

For Robyn, Alex, Oona, and Charlie,

without whose support, compassion, dedication, and love throughout the years I never even would have even started on this journey, let alone managed to finish it. You all have made me the man I am today.

Contents

List of Figures

List of Tables

Abstract

Upper Boundary Condition for Asteroseismological Modelling of Solar-type Stars

by K. Christopher Cooke

We present a grid of line blanketed spherical LTE model atmospheres and high resolution extinction spectra for use in interpolating an accurate outer boundary condition for asteroseismology calculations at arbitrary $T_{\rm eff}$ and $\log g$. We investigate the accuracy of four interpolation methods by interpolating within our grid to solar values of $T_{\rm eff}$ and $\log g$ and comparing the results to an exact solar model. We test the impact of the resolution of our grid on the accuracy of the interpolations by performing linear interpolations within our grid at different sampling rates in $T_{\rm eff}$ and $\log g$. We test whether interpolating $\kappa_{\rm R}$ within our grid and computing $\tau_{\rm R}$ or calculating $\tau_{\rm R}$ for each model and interpolating it directly produces more accurate results. We also present a NLTE exact solar model and compare the boundary condition resulting from it to those of the LTE exact model.

August 14, 2013

Chapter 1

Introduction

1.1 Background

Astronomy is often considered to be one of the oldest of the sciences, with roots stretching back to prehistoric times. For the majority of that time, however, it can be argued that astronomy was not a proper science. Instead, it existed in the realm of time keeping, uranography, natural history, or religion. It was only in the 17th century, when the rise of modern mathematics and the collection of high precision astronomical observations conspired to allow astronomers to directly compare theories on the nature of the cosmos to the cosmos itself, that astronomy became a rigorous scientific endeavour. Since that time, advances in mathematical methods have allowed for the creation of increasingly detailed and complex astrophysical theory, while the engineering of new technologies has permitted testing of these theories through both the steady refinement in precision astronomical observations and the introduction of entirely new kinds of observations.

The science of astronomy, born as it was alongside physics and chemistry, has evolved in lock-step with the other natural sciences. The study of the spectrum of light, first performed by Sir Isaac Newton, led to the invention of the spectroscope and the discovery of dark lines in the spectrum of the Sun by Joseph von Fraunhofer in 1814. Fifty-five years later, in 1859, Gustav Kirchoff and Robert Bunsen discovered the spectral fingerprints of the chemical elements and identified

Fraunhofer's lines with common chemical substances. In doing so, Kirchoff and Bunsen gave birth to modern observational stellar astrophysics. Unfortunately, only the very outermost layers of stars are observable using traditional astronomical instruments. Beneath the photosphere, colloquially defined as the visible surface of a star, stellar atmospheres are largely opaque to direct observation.

Leighton et al. (1962) detected periodic variations in the radial velocity and brightness of the solar surface. These variations have come to be known as the "five-minute oscillations" because they have a characteristic period of approximately 300 seconds. It would take nearly a decade for the nature of the oscillations to be understood. Ulrich (1970) and Leibacher & Stein (1971) suggested that the oscillations were the result of standing acoustic waves, or pressure waves, ringing throughout the solar interior, effectively opening the door for their use in probing the interior structure of the Sun.

With the discovery and classification of the modal structure of the five-minute oscillations (Deubner, 1975; Claverie et al., 1979; Duvall & Harvey, 1983) it has been possible to probe the global structure of the Sun. By comparing the observed frequency modes of the Solar surface to those predicted by theoretical models, it is now possible to directly compare models of the Solar interior to empirical observations. While theoretical predictions for the values of low frequency oscillations have been consistent with observations, the predictions have been shown to deviate from observations at higher frequencies. The deviation at high frequencies has been attributed to improper modelling of the near surface layers of the Sun (Guenther et al., 1992; Christensen-Dalsgaard et al., 1996; Christensen-Dalsgaard & Thompson, 1997), as nearly all published stellar structure models and asteroseismological models use highly simplified $T_{\rm kin}(\tau_{\rm R})$ relationships, such as those found using grey atmospheres or empirical solar atmospheres such as that of Krishna Swamy (1966), to set their outer boundary conditions.

In stellar structure modelling, the outer boundary condition is commonly taken to be the photosphere, which is customarily defined as the layer in a star's atmosphere where its effective temperature, $T_{\rm eff}$, is equal to the kinetic temperature of the surrounding gas, $T_{\rm kin}$. Here $T_{\rm eff}$ is

defined as the temperature – expressed mathematically by the Stefan-Boltzmann law,

$$L = 4\pi R^2 \sigma T_{\rm eff}^4 \tag{1.1}$$

where L is the bolometric luminosity of the star, R is the geometric radius of the star, and σ is the Stefan-Boltzmann constant – at which a true black body would radiate the same bolometric flux as the star. In the Krishna Swamy 1966 atmosphere the photosphere is found at $\tau_{\rm R}$ = 0.312156330, where $\tau_{\rm R}$ is the Rosseland mean optical depth, while in grey atmospheres utilizing the Eddington approximation, the photosphere is set at $\tau_{\rm R}$ = 2/3 (Demarque et al., 2008).

Throughout this thesis we calculate the kinetic temperature structure as a function of the Rosseland mean optical depth, the $T_{\rm kin}(\tau_{\rm R})$ relationship, for line-blanketed (*i.e.* non-grey) model stellar atmospheres, which do not necessarily have $T_{\rm eff}$ = $T_{\rm kin}$ at $\tau_{\rm R}$ = 2/3. In order to maintain a common measure of comparison across models, however, we focus our analysis on $\tau_{\rm R}$ = 2/3 in general, and $T_{\rm kin}(\tau_{\rm R} = 2/3)$ in particular.

While attempts have been made to compensate for these "near-surface effects" through a variety of means (examples include improving solar models through inclusion of turbulence (Li et al., 2002) and developing semi-empirical corrections to the observed oscillation frequencies (Kjeldsen et al., 2008)), they have largely been stop-gap measures made in lieu of utilizing detailed treatments of convection and the solar atmosphere near the upper boundary. Line blanketed solar atmosphere models date to the 1940s (Strömgren, 1940; Barbier, 1946), and grids of stellar atmosphere models for a range of $T_{\rm eff}$ and surface gravities, $\log g$, followed shortly thereafter (Ströemgren et al., 1944; Rudkjobing, 1947). The computation of detailed line blanketed stellar atmosphere models is computationally expensive, however, compared with the construction of stellar stellar interior models. That makes the use of modern model atmospheres inconvenient for use in stellar evolution codes, where details such as the $T_{\rm kin}(\tau_{\rm R})$ structure of the atmosphere are needed on demand for arbitrary values of $T_{\rm eff}$ and $\log g$ in order to provide accurate upper boundary conditions for the thousands of stellar structure models used to compute the evolution and seismology of a star.

Several studies have investigated the use of model stellar atmosphere structures as an upper boundary condition for stellar interior models, none of which have compared asteroseismological oscillation modes to observations, nor to other models. Morel et al. (1994) compared the radiative flux found from the diffusion approximation, as used in stellar interior modelling, to the values calculated from the ATLAS9 model atmospheres of Kurucz et al. (1991) and found that the fluxes agreed for $\tau_{\rm R} \geq 10$ in solar-type stars. However, that does not appear to be a necessary condition for fitting a detailed atmosphere onto a stellar interior model. Montalbán et al. (2001) computed evolutionary tracks for low metallicity (metal mass fraction $Z = 2 \times 10^{-4}$) 0.8 $\mathrm{M}_{\odot}$ stars joined to ATLAS9 model atmospheres at values of $\tau_{\rm R}$ = 1, 10, and 100. Two sets of interior and atmospheric models were computed, one using Mixing Length Theory, and another using Full Spectrum Turbulence. They found that, so long as convection was treated using the same formulation in the interior as in the atmosphere, the evolutionary tracks differed very little when the interior model's outer boundary conditions were set at different values of $\tau_{\rm R}$. For models utilizing Mixing Length Theory, in particular, the evolutionary tracks are nearly indistinguishable from the main sequence through the sub-giant branch of the HR diagram, with the red giant branch showing a spread in $T_{\rm eff}$ of approximately 30 K at the tip.

More recently, VandenBerg et al. (2008) used the MARCS stellar atmosphere code (Gustafsson et al., 2008) to produce line blanketed stellar atmospheres having [Fe/H] values of both 0.0 and -2.0, using solar elemental abundances from both Aufdenberg et al. (1998) and Asplund et al. (2005), under the assumption of local thermodynamic equilibrium for use in setting the outer boundary conditions of stellar evolution models, and tested $\tau_{\rm R}$ = 2/3 (the photosphere) and 100 as the outer boundary point. Care was taken to use the same abundances of He and the most important heavy metals, as well as the same opacities and thermodynamics, in the atmospheric and interior models. For comparison, evolutionary tracks of models utilizing a grey atmosphere and the Krishna Swamy (1966) (KS66) atmosphere were also calculated. They found the evolutionary tracks for the $\tau_{\rm R}$ = 2/3 and $\tau_{\rm R}$ = 100 fitting points were nearly identical, and concluded that, in the case of a 1 $\mathrm{M}_{\odot}$ star with solar metallicity, the $T_{\rm eff}$ scale is essentially independent of the choice of $\tau_{\rm R}$ for the outer

boundary.

The evolutionary tracks created using the MARCS atmosphere were found to lie "very close" to those found using the grey atmosphere, with the MARCS model atmospheres leading to a red giant branch that has a $\sim$20 K warmer $T_{\rm eff}$ than the grey atmosphere. The red giant branch calculated using the KS66 atmosphere was found to be $\sim$150 K hotter than those found using the MARCS atmosphere. The comparisons were performed utilizing the appropriate mixing length parameters, α, to satisfy solar constraints ($\alpha = 2.0$ for KS66, 1.71 for the grey atmosphere, and 1.80 for the MARCS atmosphere). Comparisons were also made between models using MARCS atmospheres that employed macroturbulence and MARCS atmospheres that did not, with the evolutionary tracks diverging only along the red giant branch, and even then only with a spread of $\sim$30 K in $T_{\rm eff}$.

While stellar structure and evolution calculations are insensitive to the changes introduced by using line blanketed stellar atmosphere models, the question is still open as to whether such a detailed treatment of the structure of the near-surface layers of stars will improve the agreement between predicted and observed stellar surface oscillation frequencies. Moreover, to date only model atmospheres computed under the assumption of local thermodynamic equilibrium (LTE) have been used in such studies. in LTE model atmospheres the strengths of absorption lines in the spectral energy distribution (SED) are calculated using Maxwellian-Boltzmann and Saha-Boltzmann statistics, which depend only on the local kinetic temperature of the gas to determine the energy level populations of atoms, ions, and molecules in the stellar atmosphere. A more realistic treatment of the atmosphere beyond the inclusion of line blanketing, i.e. atmospheres computed without the simplifying assumption of LTE and that account for deviations from the Boltmann, Saha, and Planck distributions caused by non-local radiation transfer, has yet to be studied as an outer boundary condition for stellar structure models.

Recently, Gruberbauer et al. (2012) developed a Bayesian analytical treatment for asteroseismological grid fitting, and in doing so removed the need to apply semi-empirical corrections to the observations. Using their Bayesian methods to study asteroseismological models of the Sun, Gruberbauer & Guenther (2013) found indications of systematic errors in stellar

evolutionary models.

In this thesis we use a grid of line-blanketed LTE stellar atmospheres, and a single non-LTE solar atmosphere, to generate high resolution opacity spectra for stars with $T_{\rm eff}$ and $\log g$ values similar to those of the Sun, from which we can quickly interpolate temperature structures on the fly for use in stellar models of near solar-type stars as they evolve on the main sequence. In Chapter 2, we describe the computational modelling of, and the methods used to interpolate within, our grid of models. In Chapter 3, we present the results of comparing models of the solar atmosphere computed by interpolating within our grid of models to an exact LTE solar atmosphere, and of comparing our exact NLTE solar atmosphere to the exact LTE solar atmosphere. Finally, in Chapter 4, we reiterate our main conclusions, and discuss the possible directions in which future research could continue.

Chapter 2

Methods

2.1 Key Concepts

2.1.1 Local thermodynamic equilibrium

It is often convenient to consider stars as black body radiators, and so it is assumed, to first approximation, that stars are in strict thermodynamic equilibrium (STE). Under STE the distribution of energy levels for both gas particles and photons can be determined entirely by T_{kin}. Under the condition of strict thermodynamic equilibrium a system is isothermal and experiences no net flow of energy. This is obviously not the case for stars, as energy is observed to flow outward form the stellar interior and through the surface by convection and electromagnetic radiation. For this energy to be transported from the inner regions of a star to the outer regions, a temperature gradient must exist, such that it is hotter deeper in the stellar interior than it is near the stellar surface.

While stars are not in strict global thermodynamic equilibrium, it is still possible to use the value of T_{kin}at a given location to describe an approximation of thermodynamic equilibrium over a localized region. This approximation, known as local thermodynamic equilibrium (LTE), is valid so long as the change in temperature over the local mean free path of a photon at that location, ℓ, can be treated as negligible. When that occurs, radiation is effectively trapped in the local environment

long enough to come into thermal equilibrium with the surrounding matter, and thermodynamic equilibrium is achieved locally.

The kinetic temperature of the gas, $T_{\rm kin}$, is defined by the Maxwell-Boltzmann distribution of particle speeds,

$$\frac{n(v)}{N}dv = 4\pi v^2 \left(\frac{m}{2\pi k_{\rm B} T_{\rm kin}}\right)^{2/3} e^{\frac{-mv^2}{2kT_{\rm kin}}} dv, \tag{2.1}$$

where $n(v)dv$ is the number of particles of mass m with speeds between v and $v + dv$, N is the total number of particles in the system, and $k_{\rm B}$ is the Boltzmann constant. In LTE, as in STE, $T_{\rm kin}$is set equal to the excitation temperature, $T_{\rm exc}$, as defined by the Boltzmann distribution of excitation states,

$$\frac{N_i}{N} = \frac{g_i e^{-E_i/(k_{\rm B}T_{\rm exc})}}{\sum_{j=1}^{\infty} g_j e^{-E_j/(k_{\rm B}T_{\rm exc})}}, \tag{2.2}$$

where N_i is the number of particles occupying the ith excitation state, $N = \sum_i N_i$, E_i the energy of the ith excitation state, and g_i is the degeneracy of the ith state, as well as to the ionization temperature, $T_{\rm ion}$, as defined by the Saha distribution of ionization states,

$$\frac{n_{k+1,1}}{n_{k,1}} n_e = \frac{g_{k+1,1}}{g_{k,1}} g_e \left(\frac{2\pi m_e k_{\rm B} T_{\rm ion}}{h^2}\right)^{\frac{3}{2}} e^{-\frac{\chi_k}{k_{\rm B}T_{\rm ion}}}, \tag{2.3}$$

where $\frac{n_{k+1,1}}{n_{k,1}}$ is the population ratio between the ground state of the kth and $(k + 1)$th ionization stages, n_e is the electron density, $g_{k,1}$ and $g_{k+1,1}$ are the ground state degeneracies of the kth and $(k+1)$th ionization stages, respectively, g_e = 2 and is the degeneracy of the electron in a given energy level, m_e is the mass of the electron, h is Planck's constant, and χ_k is the ground state ionization energy of the kth ionization stage and also to the radiation temperature, $T_{\rm rad}$, which is defined by the Planck distribution of photon wavelengths,

$$B_\lambda = \frac{2hc^2}{\lambda^5} \frac{1}{e^{\frac{hc}{\lambda k_{\rm B} T_{\rm rad}}} - 1} \tag{2.4}$$

where B_λ is the intensity of photons of wavelength λ.

2.1.2 The Rosseland mean opacity

Deep in the atmosphere of a star, where the mean free path of a photon is similar to that of gas particles, and where the approximation of LTE holds, it is useful to take an average of the monochromatic extinction coefficient over all wavelengths. While extinction from bound-bound (b-b) processes is not negligible, and cannot be ignored, it is useful to have the average extinction coefficient closely resemble the background continuum opacity. The appropriate average to take in this case is the Rosseland mean average of the extinction coefficients, which is a flux-weighted harmonic mean (described below) and which arises from the averaging of the radiative transport equation over all wavelengths. It is given by the equation

$$\frac{1}{\kappa_{\mathrm{R}}} = \frac{\int_0^\infty \frac{1}{\kappa_\lambda}\frac{\partial B_\lambda}{\partial T}\mathrm{d}\lambda}{\int_0^\infty \frac{\partial B_\lambda}{\partial T}\mathrm{d}\lambda}, \tag{2.5}$$

where κ_λ is the monochromatic linear extinction coefficient, $\frac{\partial B_\lambda}{\partial T}$ is the temperature derivative of the Planck function, and κ_{R} is the Rosseland mean extinction coefficient.

In stellar interior modelling, we are often interested in finding the net bolometric luminosity being radiated by a star. In an optically thick medium, such as that found in the stellar interior, that is conveniently done using the radiative diffusion equation,

$$L = -\frac{64\pi r^2 \sigma T_{\mathrm{kin}}^3}{3\kappa\rho}\frac{\partial T_{\mathrm{kin}}}{\partial r}, \tag{2.6}$$

where L is the bolometric luminosity emitted by the star, σ is the Steffan-Boltzmann constant, and κ is the grey extinction coefficient. The equation also holds for specific luminosity, $L_\lambda(\lambda)$, in the case where the specific extinction coefficient, κ_λ is substituted for κ. L is found from L_λ by integrating over all wavelengths. Doing so, one finds that the appropriate grey opacity coefficient to use in the diffusion equation is the Rosseland mean extinction coefficient, Eq. 2.5.

2.1.3 Optical depth

In the atmosphere of a star, the average distance a photon of wavelength λ travels between interactions with atoms or molecules is given by its mean free path,

$$\ell_\lambda = \frac{1}{\kappa_\lambda}, \tag{2.7}$$

where ℓ_λ has units of cm, and κ_λ (cm^{-1}) can be treated as the fraction of photons of wavelength λ (Å) that are removed from a beam (either by absorption of scattering) for every centimetre travelled. It follows that

$$\mathrm{d}\tau_\lambda = -\kappa_\lambda \mathrm{d}s, \tag{2.8}$$

where $\mathrm{d}\tau_\lambda$ represents the total fraction of photons of wavelength λ that are removed from a beam passing through a medium of geometric thickness $\mathrm{d}s$.The negative sign comes from the fact that when we observe light from a star we are looking along the beam in the direction opposite to that which the photons travel.

An optical depth scale can be defined for any extinction coefficient. Just as it can be useful to define an average extinction, such as κ_R, in a stellar atmosphere, it is also convenient to use such an average extinction to define an optical depth scale. In the case of κ_R we define the corresponding Rosseland mean optical depth, τ_R (see Section 2.3 for details), which is commonly use to define the location of the photosphere of the Sun.

2.2 PHOENIX

2.2.1 The grid of models

To calculate the grid of models, we have used version 15 of the multipurpose stellar atmosphere computer code PHOENIX (Hauschildt et al., 1999). PHOENIX was designed to be very flexible,

and, in addition to stars, has been used to generate model atmospheres for novae and supernovae, accretion disks, white dwarfs, and sub-stellar objects such as brown dwarfs and planets. It is capable of calculating model stellar atmospheres of varying types: static or expanding, plane-parallel or 1D spherical geometry, line-blanketed or not, and LTE or NLTE (Aufdenberg et al., 1998). For the purposes of this thesis, PHOENIX was used to compute static, spherical, line-blanketed stellar model atmospheres and synthetic spectra under the approximation of local thermodynamic equilibrium (LTE). The models in our grid do not include the effects of rotation, magnetic fields, X-ray heating, or stellar winds, nor do they include the chromosphere and corona. The chromosphere and corona can be safely neglected because we are interested in the properties of the atmosphere at $\tau_{\rm R}$ = 2/3, which is much deeper in the atmosphere than the temperature minimum where the chromospheric temperature begins to rise. One additional non-local thermodynamic equilibrium (NLTE) model atmosphere and synthetic opacity spectrum was computed for the sake of comparison, which is discussed in Section 2.5.

The grid itself contains 28 spherical atmospheric models, each with 64 layers, spanning a range in $T_{\rm eff}$ from 5600 K to 5900 K, sampled every $\Delta T_{\rm eff} = 50$ K, and in $\log g$ from 3.5 to 5.0, sampled every $\Delta \log g = 0.5$ dex. All models in the grid are computed with a mixing length parameter, $\alpha = 1.0$, and with a microturbulent velocity dispersion, $\xi_{\rm T} = 1.0\ {\rm kms}^{-1}$. Each model atmosphere is computed with solar metallicity ($\left[\frac{\rm A}{\rm H}\right] = 0.0$) and utilize the solar abundance determinations of Grevesse & Sauval (1998) to ensure consistency with the solar interior models for which they are to act as an outer boundary condition. More recent solar abundance determinations based on three-dimensional (3D) hydrodynamical models of the Sun exist (e.g. Asplund et al. (2005) and Asplund et al. (2009)) and predict values of $\left[\frac{\rm C}{\rm H}\right]$ and $\left[\frac{\rm N}{\rm H}\right]$ that are 19% lower, and values of $\left[\frac{\rm O}{\rm H}\right]$ and $\left[\frac{\rm Ne}{\rm H}\right]$ that are 28% lower, than those recommended by Grevesse & Sauval (1998). To compute spherical models, PHOENIX requires as input the effective radius, $R_{\rm eff}$, where the standard optical depth, $\tau_{\rm STD}$, is unity (Short & Hauschildt, 2003). For our models, $\tau_{\rm STD}$ is taken as τ_{12000}, the optical depth resulting from continuous extinction processes at $\lambda = 12000$ Å. To calculate $R_{\rm eff}$, each model was assumed to have a mass of $1{\rm M}_{\odot}$. Newton's equation of universal gravitation,

$$10^{\log g} = \frac{G\mathrm{M}_{\odot}}{R_{\mathrm{eff}}^2}, \tag{2.9}$$

was then solved for R_{eff} using the necessary value of $\log g$.

2.2.2 Creating the models in PHOENIX

There are two steps to creating a model stellar atmosphere and corresponding synthetic stellar opacity spectrum in PHOENIX. The first step is to compute the vertical temperature, pressure, and density structures. For a given T_{eff}, R_{eff}, and $\log g$, PHOENIX solves the time independent, spherically symmetric, special relativistic equation of radiative transfer at all input values of τ_{STD}, and uses the conditions of thermal equilibrium and hydrostatic equilibrium to compute the kinetic temperature structure of the atmosphere.

The radiative transfer equation (RTE) is given by

$$e\frac{\partial I}{\partial r} + \frac{\partial}{\partial \mu}(fI) + g\frac{\partial}{\partial \lambda}(\lambda I) + hI = \eta - \chi I, \tag{2.10}$$

where

$$e(r,\mu) = \gamma(\mu + \beta), \tag{2.11}$$

$$f(r,\mu) = \gamma(1-\mu^2)\left[\frac{1+\beta\mu}{r} - \gamma^2(\mu+\beta)\frac{\partial\beta}{\partial r}\right], \tag{2.12}$$

$$g(r,\mu) = \gamma\left[\frac{\beta(1-\mu^2)}{r} + \gamma^2\mu(\mu+\beta)\frac{\partial\beta}{\partial r}\right], \tag{2.13}$$

$$h(r,\mu) = \gamma\left[\frac{\beta(1-\mu^2)}{r} + \gamma^2(1+\mu^2+2\beta\mu)\frac{\partial\beta}{\partial r}\right], \tag{2.14}$$

and r is the radial coordinate, $I(r,\mu,\lambda)$ is the specific intensity scaled by r^2, μ is the cosine of the direction angle such that $\mu = \cos\phi$, β is the velocity as a fraction of the speed of light in a vacuum, $\beta = v/c$, γ is the Lorentz factor, $\gamma = (1-\beta^2)^{-1/2}$, $\eta(r,\lambda)$ is the emissivity, and $\chi(r,\lambda)$ is the total extinction coefficient. In this thesis we are only considering static atmospheres, and so we are

solving the RTE for the case where $\beta = 0$ and $\gamma = 1$. The boundary conditions used to solve the RTE are $I(r, \mu = -1, \lambda) = 0$ at $\tau_{\rm STD} = 0$ and $I(r, \mu = 1, \lambda) = B_\lambda$ at $\tau_{\rm STD} = \tau_{\rm max}$, which applies when there is no radiation incident on the star's surface, and the outgoing intensity at the bottom of the atmosphere is given by the Planck function.

PHOENIX solves the radiative transfer equation and the vertical temperature, pressure, and density profiles iteratively, with each iteration introducing temperature corrections until the structure converges and the user-selected number of iterations is reached. Convergence is achieved when the relative difference between the bolometric flux calculated by PHOENIX and that predicted from exact thermal equilibrium, $F = \sigma T_{\rm eff}^4$, is $\leq 1\%$. For our LTE models convergence was achieved in 10 iterations or fewer.

For our purposes, the process involved taking a pre-existing PHOENIX stellar atmospheric structure model that had properties close to those we wished to investigate and seeding the structure convergence calculations with it. That allowed us to keep the number of iterations small and increased the chance of the structure converging.

The next step was to run PHOENIX in its spectral synthesis mode. To do that, the wavelengths, λ, and wavelength spacing, $\Delta\lambda$, over which the star's spectrum is to be sampled is input into PHOENIX. To ensure our spectra were fully sampled, our sampling was chosen such that the effective spectral resolution, $\lambda/\Delta\lambda$, was held at a value of at least 2×10^5 throughout the spectrum. The sampling over the full spectrum is given in Table 2.1. We ran PHOENIX in a special mode such that it printed out the values of κ_λ at all λ and $\tau_{\rm STD}$ values.

2.2.3 Calculating line opacities

To calculate line opacities, PHOENIX utilizes an atomic line list that includes 47 million atomic lines, and a molecular line list that includes up to 550 million molecular lines. Rather than utilizing precomputed opacity sampling tables, PHOENIX utilizes a direct opacity sampling method for both atomic and molecular lines. At the beginning of each iteration, PHOENIX selects the relevant LTE

Table 2.1: Sampling of the spectra.

Range [Å]	Sampling
2070–5000	$\Delta\lambda$ = 0.010 Å
5000–6000	$\Delta\lambda$ = 0.013 Å
6000–7000	$\Delta\lambda$ = 0.016 Å
7000–8000	$\Delta\lambda$ = 0.020 Å
8000–11000	$\Delta\lambda$ = 0.023 Å
11000–13000	$\Delta\lambda$ = 0.027 Å
13000–15000	$\Delta\lambda$ = 0.037 Å
15000–17000	$\Delta\lambda$ = 0.050 Å
17000–19000	$\Delta\lambda$ = 0.060 Å
19000–21000	$\Delta\lambda$ = 0.070 Å
21000–23000	$\Delta\lambda$ = 0.080 Å
23000–25000	$\Delta\lambda$ = 0.090 Å

lines from the atomic and molecular line lists, and sums their contributions to calculate the total line opacity at an arbitrary wavelength point. That allows PHOENIX to handle both regular and irregular wavelength grids, which is an important feature for NLTE calculations. It also permits the use of detailed and depth dependent line profiles during the iterations. It is particularly useful for computing the line opacities in cool dwarf stars, as the line forming regions in cool dwarfs can span large ranges in pressure and temperature, with the core of a line forming in different layers from the wings of the same line. Whether a line is included in that summation or not is determined by the relative strength of the line extinction coefficient, $\kappa_{\rm l}$ as compared to the extinction coefficient of the continuum at the same wavelength, $\kappa_{\rm c}$. The threshold for inclusion in the model atmosphere is an input parameter chosen by the user. In our models, as in Aufdenberg et al. (1998), it has been set to $\kappa_{\rm l}/\kappa_{\rm c} = 10^{-4}$.

2.3 Computing the Rosseland mean optical depth scale

2.3.1 Computing the Rosseland mean opacity, $\kappa_{\rm R}$

With PHOENIX run in opacity output mode, the program writes out monochromatic extinction coefficients, $\kappa_{\lambda_{\rm i}}$ (units: $\rm cm^{-1}$), computed for a variety of physical processes, separated into different categories by the code, at each sampled wavelength in the spectrum, at each of the 64 layers of the atmosphere. The categories include: absorption by continuous processes such as atomic b-f transitions and H^- ionization; scattering resulting from continuous processes; strong atomic lines caused by absorption, modelled using Voigt profiles; weaker atomic lines caused by absorption, modelled using Gaussian profiles; strong atomic lines caused by scattering events, modelled using Voigt profiles; weaker atomic lines caused by scattering events, modelled using Gaussian profiles; strong molecular lines caused by absorption, modelled using Voigt profiles; weaker molecular lines caused by absorption, modelled using Gaussian profiles; strong molecular lines caused by scattering events, modelled using Voigt profiles; and weaker molecular lines caused by scattering events, modelled using Gaussian profiles. There is also a separate category, which is neglected in the LTE models but is important in the NLTE model discussed in Section 2.5, that takes into account departures from LTE values for the extinction coefficients. For the 890115 sampled wavelengths in our spectra, that produces over 5×10^8 linear extinction coefficients per star. They are used to calculate the value of the Rosseland mean extinction coefficient at each of the 64 layers of the atmosphere. Using Fortran 2003, we developed a code to solve the finite difference form of the Rosseland mean opacity equation, 2.5:

$$\frac{1}{\kappa_{\rm R}} = \frac{\sum\limits_{\rm i} \frac{1}{\kappa_{\lambda_{\rm i}}} \frac{\partial B_{\lambda_{\rm i}}}{\partial T} \Delta\lambda_{\rm i}}{\sum\limits_{\rm i} \frac{\partial B_{\lambda_{\rm i}}}{\partial T} \Delta\lambda_{\rm i}}, \tag{2.15}$$

where the sum is over the range in Table 2.1.

Here, $\kappa_{\rm R}$ is the Rosseland mean extinction coefficient, $\Delta\lambda$ is the difference between the

currently sampled wavelength and the previously sampled wavelength, and the partial derivative $\frac{\partial B_\lambda}{\partial T}$ is the rate at which the Planck function at the wavelength of interest changes with temperature in the star's atmosphere. $\frac{\partial B_\lambda}{\partial T}$ can be solved analytically to find

$$\frac{\partial B_\lambda}{\partial T} = \frac{2h^2c^3}{kT^2\lambda^6}\left[\frac{e^{(\frac{ch}{\lambda k_{\rm B}T})}}{(e^{(\frac{ch}{\lambda k_{\rm B}T})}-1)^2}\right], \tag{2.16}$$

where $k_{\rm B}$ is the Boltzmann constant. The equation that our code ultimately solves takes the form

$$\frac{1}{\kappa_{\rm R}} = \frac{\sum_{\rm i}\frac{1}{\kappa_{\lambda_{\rm i}}\lambda_{\rm i}^6}\left[\frac{e^{(\frac{ch}{\lambda_{\rm i}k_BT})}}{(e^{(\frac{ch}{\lambda_{\rm i}k_{\rm B}T})}-1)^2}\right]\Delta\lambda}{\sum_{\rm i}\frac{1}{\lambda_{\rm i}^6}\left[\frac{e^{(\frac{ch}{\lambda_{\rm i}k_BT})}}{(e^{(\frac{ch}{\lambda_{\rm i}k_BT})}-1)^2}\right]\Delta\lambda}. \tag{2.17}$$

To solve the equation computationally, care must be taken regarding the order in which the mathematical operations are performed. Because of the finite precision of floating point representations of real numbers, multiplying terms in the wrong order can lead to values being rounded to zero. To overcome that, all values in our code are recorded in double-precision variables. The constant $\frac{ch}{k_{\rm B}}$ was pre-computed and found to be $1.43877695998\ {\rm cm}^{-1}{\rm K}^{-1}$. $T\lambda$ is then found, and the exponential $e^{\frac{ch/k_{\rm B}}{T\lambda}}$ is computed. Next, $e^{\frac{ch/k_{\rm B}}{T\lambda}}(e^{\frac{ch/k_{\rm B}}{T\lambda}}-1)^{-2}$ is found, and is multiplied by λ^{-6}. To compute the numerator, it is divided by κ_λ. Finally, $\Delta\lambda = \lambda_i - \lambda_{i-1}$ is calculated. The sum from λ = 2070 Å to 25000 Å is performed at each of the 64 layers of the atmosphere, with the result for each layer being saved in two linear arrays, kr1 and kr2, each with a dimension of 64. $\kappa_{\rm R}$, itself an array with a dimension of 64, is found by dividing the array kr2 by the array kr1.

To verify that $\kappa_{\rm R}$ is being calculated correctly for the stellar atmosphere, we calculated it over a small waveband and confirmed that $\kappa_{\rm R}$ was approximately equal to the background continuum extinction. Figure 2.1 shows κ_λ, in red, and $\kappa_{\rm R}$, in blue, over the range 7500 Å $\leq \lambda \leq$ 7505 Å. As expected, $\kappa_{\rm R}$, with a value of $1.66817735828 \times 10^{-8}{\rm cm}^{-1}$, is only slightly larger than the continuum value of κ_λ.

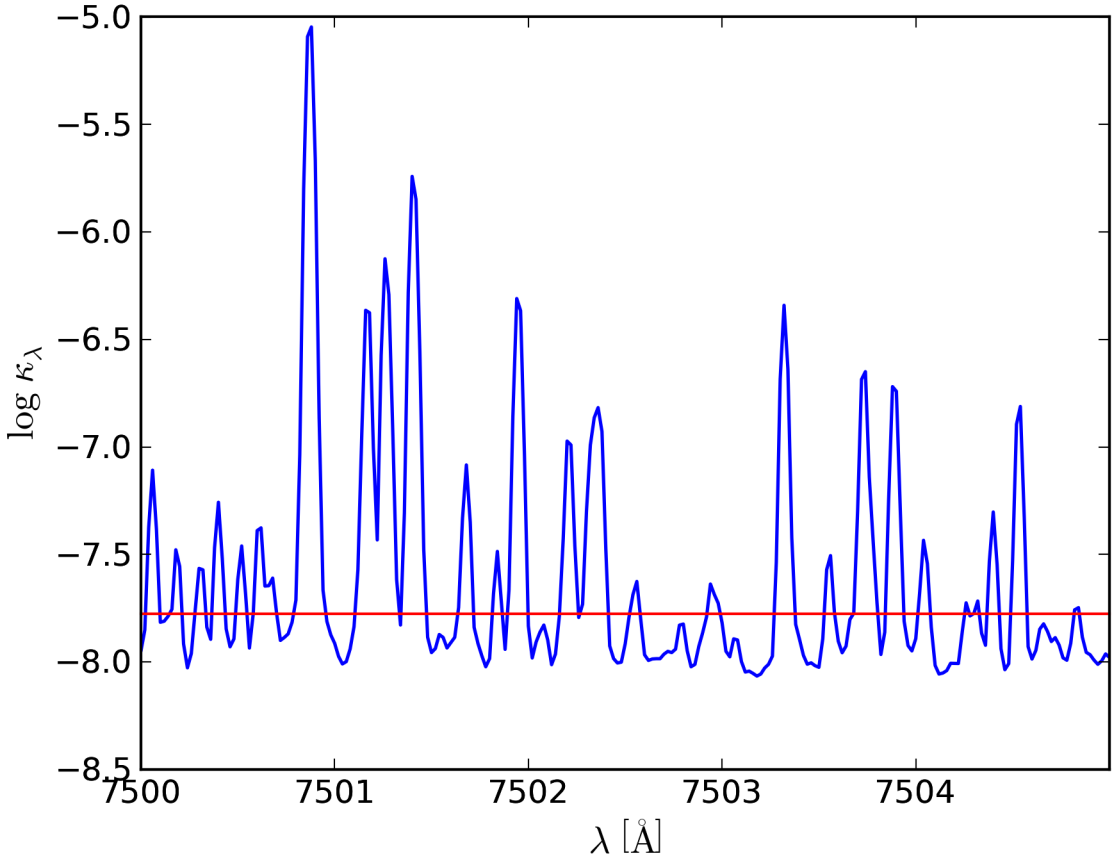

Figure 2.1: A comparison of κ_λ and $\kappa_{\rm R}$ over a limited wavelength range. The red line represents the value of $\kappa_{\rm R}$ calculated over the range $7500\text{Å} \leq \lambda \leq 7505\text{Å}$, while the blue curve shows the values of κ_λ over the same part of the spectrum.

2.3.2 Computing the Rosseland mean optical depth

Once the Rosseland mean extinction coefficients are known at the 64 depths of the stellar atmosphere, they can be integrated over the geometric depth of the atmosphere to find the Rosseland mean optical depth, $\tau_{\rm R}$, at each of the 64 depth points. Analytically, it is calculated using the equation

$$\tau_{\rm R} = -\int_{R}^{r} \kappa_{\rm R}(r){\rm d}r, \tag{2.18}$$

where $\kappa_{\rm R}$ is the volume (linear) extinction, in units of $\rm cm^{-1}$, R is the outer radius of the star measured in cm, defined at $\tau_{\rm STD}$ = 0, and r is the distance between a point in the star's atmosphere and the star's centre (also measured in cm), *i.e.* $R - r$ is the depth into the atmosphere at which $\tau_{\rm R}$ is being calculated.

To compute that, our code uses a finite difference form of equation 2.18,

$$\tau_{\rm R,n} = -\sum_{i\,=\,2}^{n} \kappa_{\rm R,i}\Delta r_{\rm i}, \tag{2.19}$$

where n is the index of the atmospheric layer, counted from the top of the atmosphere, $\Delta r_{\rm i} = r_{\rm i} - r_{\rm i-1}$, and $r_{\rm i}$ is the geometric radius of the $i^{\rm th}$. The layer $i = 1$ was neglected because it is the upper boundary condition, and has an artificially low value of $\kappa_{\rm R}$.

2.3.3 Comparison of results from the MARCS and PHOENIX codes

To check that the $T_{\rm kin}(\tau_{\rm R})$ relationship resulting from the LTE PHOENIX output is consistent with published results, we compared our output for the Sun with a pre-existing one-dimensional (1D) spherical LTE model of the solar atmosphere computed using the MARCS stellar atmosphere code (Gustafsson et al., 2008). The MARCS output consists of $T_{\rm kin}$, $\tau_{\rm R}$, and the Rosseland mean of the mass extinction coefficient in units of $\rm cm^2 g^{-1}$, $\kappa_{\rm R,m}$, among other values. Our PHOENIX output included $T_{\rm kin}$, the mass density, ρ, and the linear extinction coefficient, κ_{λ}. To compare the MARCS

and PHOENIX extinction coefficients, PHOENIX's linear extinction coefficients were converted to mass extinction coefficients, using the formula

$$\kappa_{\mathrm{R,m}} = \frac{\kappa_{\mathrm{R}}}{\rho}. \tag{2.20}$$

Figure 2.2 shows the relationship between T_{kin} and $\kappa_{\mathrm{R,m}}$ for the MARCS model, shown in red, and the PHOENIX model, shown in blue. Figure 2.3 shows the predicted T_{kin} profile between the top of the atmosphere, $\tau_{\mathrm{R}} \approx 0$, and $\tau_{\mathrm{R}} \approx 100$ for the two models, where the colours used are the same as in Figure 2.2. The agreement between the two models is very good, illustrating that the physics and computations underlying the PHOENIX values are consistent with those used in the literature.

The intercepts between the $T(\tau_{\mathrm{R}})$ relationships and the vertical black line represent the value of T_{kin} at $\tau_{\mathrm{R}} = 2/3$ which, under the approximation of LTE and a grey opacity, defines the value of T_{eff}. The MARCS relation intercepts at a value of $T_{\mathrm{kin}} \approx 5916$ K, while the PHOENIX relationship intercepts at a value of $T_{\mathrm{kin}} \approx 5780$ K. The PHOENIX model had $T_{\mathrm{eff}} = 5780$ K as an input parameter, whereas the MARCS model had $T_{\mathrm{eff}} \approx 5777$ K as an input parameter.

2.4 Interpolating within the grid

We are interested in interpolating several quantities, namely T_{kin}, κ_{R}, τ_{R}, the mass density, ρ, the radial position R, the gas pressure, P_{gas}, and the electron pressure, P_{e}, each of which are functions of τ_{STD}, T_{eff}, and $\log g$. When interpolating models within the grid, we are interpolating the 64 values of each of the quantities within T_{eff} and $\log g$ at each value of τ_{STD}. When interpolating these quantities within a model, we are interpolating them among the 64 values of τ_{STD} over which each quantity is sampled.

We exploit the fact that PHOENIX uses τ_{STD} as the independent variable for the vertical structure of the models, and we have used the same τ_{STD} values for each model in the grid. This

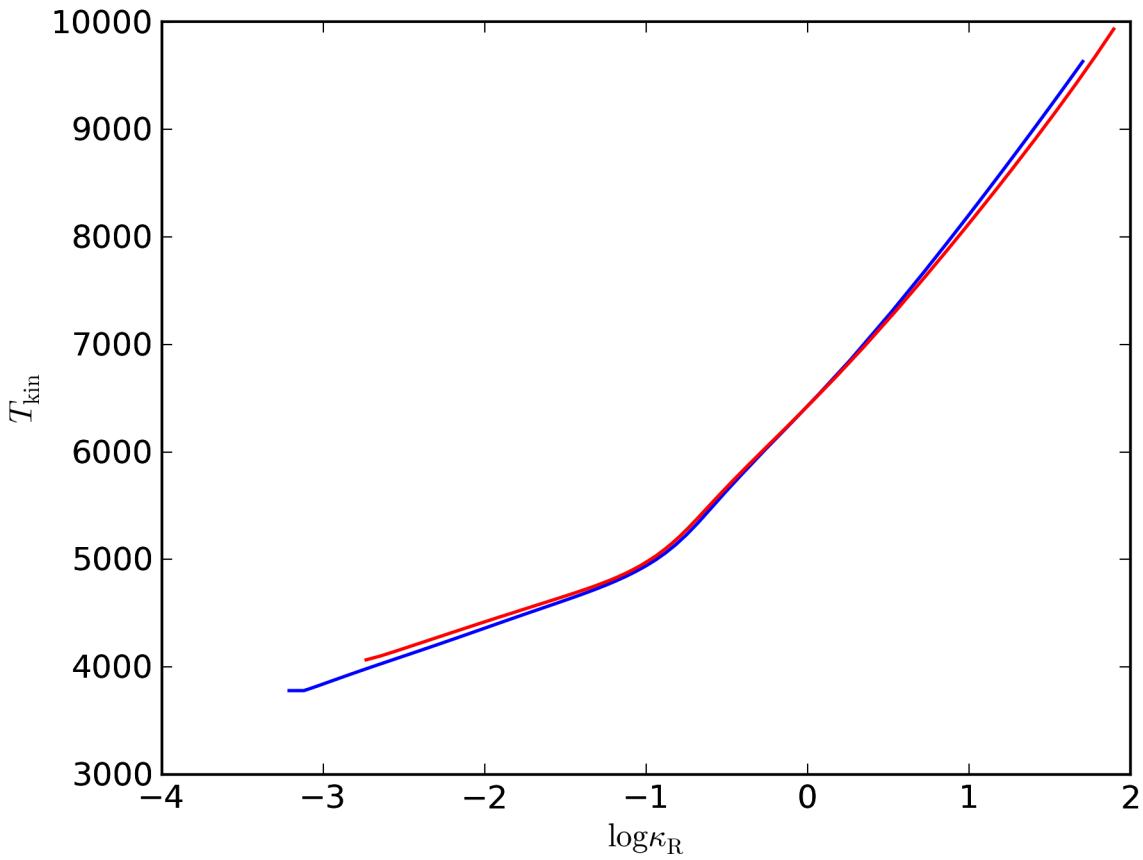

Figure 2.2: The computed relationship between $T_{\rm kin}$ and $\kappa_{\rm R}$ for the Sun. The red line represents the predictions from the MARCS model, while the blue line is the prediction from PHOENIX.

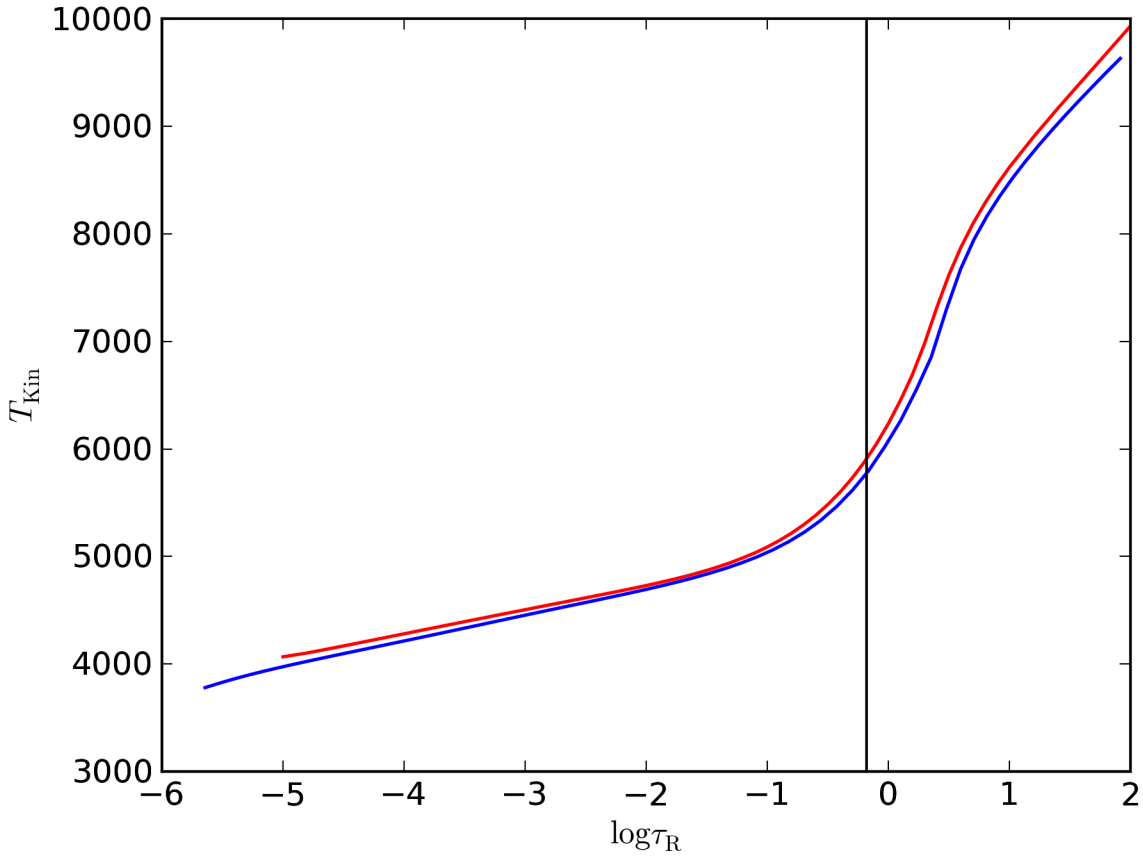

Figure 2.3: Computed $\mathrm{T}(\tau_{\rm R})$ relationships for the Sun. The red line represents the predictions from the MARCS model, while the blue line is the prediction from PHOENIX. The black vertical line illustrates the value $\tau_{\rm R} = 2/3$.

is particularly convenient for us, as it allows us to interpolate $T_{\rm kin}(\tau_{\rm STD})$, $\kappa_{\rm R}(\tau_{\rm STD})$, and $\tau_{\rm R}(\tau_{\rm STD})$ directly, without first having to interpolate them onto a common independent variable.

As we have interpolated $\kappa_{\rm R}(\tau_{\rm STD})$ and $R(\tau_{\rm STD})$ in addition to $\tau_{\rm R}(\tau_{\rm STD})$, it is possible to compute $\tau_{\rm R}$ from the interpolated values of $\kappa_{\rm R}$ and R and compare the results to the values of $\tau_{\rm R}$ which have been interpolated within the grid. That is done in Section 2.4.4.

2.4.1 Interpolation methods

We explored four different methods of interpolating the quantities within our grid of models: linear, quadratic, least-squares quadratic, and cubic spline interpolation.

Linear and quadratic interpolations

We investigated two-point and three-point interpolation methods. The linear interpolation takes two ordered pairs and determines a value of the ordinate for an input abscissa using a straight line fit connecting the two ordered values. The quadratic interpolation takes three ordered pairs, $(x_{\rm i-1}, y_{\rm i-1})$, $(x_{\rm i}, y_{\rm i})$, and $(x_{\rm i+1}, y_{\rm i+1})$, and determines the value at $y_{\rm out}$ for the point of interest, $x_{\rm out}$, which is defined such that $x_{\rm i} \leq x_{\rm out} \leq x_{\rm i+1}$, using a quadratic fit to the trio of points.

Least-squares quadratic interpolation

We also investigated a quadratic interpolation method that uses four data points, $(x_{\rm i-1}, y_{\rm i-1})$, $(x_{\rm i}, y_{\rm i})$, $(x_{\rm i+1}, y_{\rm i+1})$, and $(x_{\rm i+2}, y_{\rm i+2})$ distributed around $x_{\rm out}$, i.e. $x_{\rm i} \leq x_{\rm out} \leq x_{\rm i+1}$. The method finds a least-squares quadratic fit to the four points surrounding $x_{\rm out}$, and then computes $y_{\rm out}(x_{\rm out})$ from the parabola.

Cubic spline interpolation

We also investigated an exact, albeit piecewise, four-point interpolation in the form of a cubic spline. A cubic spline is a piecewise cubic curve with continuous first and second derivatives.

There are several methods that can be used to find cubic splines from sets of three or more data points. The method utilized by the library we used solves the system of equations to find the exact cubic polynomial defined by the four data points, $(x_{\mathrm{i}-1}, y_{\mathrm{i}-1})$, $(x_{\mathrm{i}}, y_{\mathrm{i}})$, $(x_{\mathrm{i}+1}, y_{\mathrm{i}+1})$, and $(x_{\mathrm{i}+2}, y_{\mathrm{i}+2})$ distributed around the desired abscissa, i.e. $x_{\mathrm{i}} \leq x_{\mathrm{out}} \leq x_{\mathrm{i}+1}$. The process is repeated for every interval $(x_{\mathrm{i}}, x_{\mathrm{i}+1})$ in the data set, resulting in an interpolated function that is smooth and twice differentiable.

Basic Interpolation Benchmarks

Benchmarks were run on each method listed above by performing a representative interpolation within our grid of models 100,000 times and measuring the amount of time taken and memory used for the procedure to finish. Each interpolation among the models involved 11 calls to the desired interpolation function.

The linear interpolation method was found to take an average of 4.91 ms of CPU time and a maximum of 2624 byes of memory per grid interpolation. The quadratic method similarly used a maximum of 2624 byes of memory, but saw the average CPU time per grid interpolation jump by 34% relative to the linear method to 6.59 ms. Interpolation by the least-squares quadratic method fared the worst in the benchmarks, with an average CPU time per grid interpolation of 18.30 ms – an increase of 273% compared to the linear interpolation method – and a maximum memory usage of 4768 bytes, while interpolation by cubic splines exhibited middling results of 3488 bytes of memory used at peak memory usage and an average CPU run time of 8.90 ms (an increase of 81% over the linear method) per grid interpolation.

2.4.2 Interpolation order

As we are interpolating among a two-dimensional (2D) grid of stellar atmospheres, interpolations needed to be performed in both T_{eff} and $\log g$. Given the relatively small size of the grid, it was determined that a two-step interpolation method was most appropriate.

To maintain consistency, bilinear, biquadratic, and bicubic interpolations were explored. The 2D interpolation methods involve performing a linear, quadratic, or cubic interpolation, respectively, first along one axis, and then performing an interpolation of the same order along the second axis.

To determine whether the order in which our interpolations were performed had an impact on the final result, PHOENIX was used to compute a set of 12 additional model atmospheres. Seven of the models were made holding $\log g$ constant at $\log g_{\odot} = 4.44$ and varying $T_{\rm eff}$ from 5600 K to 5900 K in intervals of $\Delta T_{\rm eff} = 50$ K, while four more were made holding $T_{\rm eff}$ constant at $T_{\rm eff,\odot} = 5780$ K and varying $\log g$ from 3.5 to 5.0 in intervals of $\Delta \log g = 0.5$. One final model was produced using the exact values of the Sun, $T_{\rm eff,\odot}$ = 5780 K, $\log g_{\odot}$ = 4.44.

It is worth noting that the step size in surface gravity, g, in our grid is large compared to the step size in $T_{\rm eff}$. $\Delta \log g = 0.5$ represents a change in g by a factor of $\sim$312%, where $\Delta T_{\rm eff} = 100K$ represents a change in $T_{\rm eff}$ of $\sim$2%. The grid sampling rates are typical of published model grids, as stellar spectra are significantly more sensitive to changes in $T_{\rm eff}$ than changes in g (let alone $\log g$). It is readily seen in the Steffan-Boltzmann law ($L \propto gT^4$) and the diffusion equation ($L \propto gT^3$), among others.

Interpolating $T_{\rm kin}(\tau_{\rm STD})$ within $T_{\rm eff}$ to $T_{\rm eff}$ = $T_{\rm eff,\odot}$ with $\log g$ held constant at $\log g_{\odot}$ resulted in a root-mean-square (RMS) deviation of interpolated to exact $T_{\rm kin}(\tau_{\rm STD})$, σ_T, of 0.006%, while interpolating $T_{\rm kin}(\tau_{\rm STD})$ among $\log g$ to $\log g$ = $\log g_{\odot}$ with $T_{\rm eff}$ held constant at 5780 K resulted in σ_T of 0.012%. It was therefore determined that interpolations within the grid of models was least sensitive to interpolations among $T_{\rm eff}$, therefore interpolations within the grid were performed within $T_{\rm eff}$ first.

Interpolations to $T_{\rm eff,\odot}$ were performed within $T_{\rm eff}$ for each value of $\log g$ in the grid using each of the methods described above. They were compared with the values from the exact models computed in PHOENIX with $T_{\rm eff} = 5780$K and the corresponding value of $\log g$. They were then interpolated over $\log g$ to find the values at the solar values of $T_{\rm eff}$ and $\log g$. Finally, the resulting values were compared to those from the exact solar model. The process was then repeated, interpolating first over $\log g$ and then over $T_{\rm eff}$. The results are presented in Table 2.2, from which

we can see that for each interpolation method, the results differ negligibly regardless of the order in which the interpolations are performed. For the sake of consistency, all 2D interpolations in this thesis are performed over $T_{\rm eff}$ followed by those in $\log g$.

2.4.3 Comparison of the interpolation methods

As can be seen from Table 2.2, with the exception of the least-squares quadratic method, increasing the number of data points over which an interpolation is performed increases, on average, the agreement between the interpolated atmosphere's structure and that of the exact solar model. That holds in general throughout the atmosphere. Figure 2.4 shows the relative difference between $T_{\rm kin}(\tau_{\rm STD})$ from the exact solar atmosphere and the values found from the four interpolation methods discussed in section 2.4. The cubic spline interpolation, shown in green, is nearest the exact solar value almost throughout the entire atmosphere. The results from the linear interpolation, illustrated with the blue line, and the quadratic interpolation, shown in red, are largely nearly indistinguishable, and are intermediate between the cubic spline results and those of the least-squares quadratic interpolation, shown in orange.

Similar results are seen when we examine the structure of other properties of the atmosphere. Figure 2.5 shows the relative differences from comparing the radial height values, $R(\tau_{\rm STD})$, that result from the different interpolation methods to that from the exact solar model. Each interpolation method misestimates the radial position of the atmospheric layers by a constant factor, with the quadratic and cubic spline methods being most accurate, and the least-squares quadratic method being the least accurate. Of the four interpolation methods, only linear interpolation overestimates the radius of the star, and does so by less than 2%.

Figure 2.6 shows the relative differences between the interpolated Rosseland mean opacities, $\kappa_{\rm R}(\tau_{\rm STD})$, and those from the exact solar model. Once again, the values arrived at via least-squares quadratic interpolation fare the worst, deviating from the exact solar value by up to 12%. As expected, linear interpolation is next best, over-estimating the exact solar values by at most 5.5%,

Table 2.2: Root Mean Square Deviations of the relative differences comparing modelled and interpolated stellar atmosphere properties at $\log g$ = 4.44, $T_{\rm eff}$ = 5780 K.

Over $T_{\rm eff}$ then $\log g$			Over $\log g$ then $T_{\rm eff}$	
Variable	σ	$\sigma(\tau_{\rm STD} < 1)$	σ	$\sigma(\tau_{\rm STD} < 1)$
Linear Interpolation:			Linear Interpolation:	
$T_{\rm kin}$	0.030 %	0.032 %	0.030 %	0.032 %
$\kappa_{\rm R}$	5.136 %	5.293 %	5.136 %	5.293 %
$\tau_{\rm R}$	0.039 %	0.037 %	0.039 %	0.037 %
ρ	2.171 %	2.010 %	2.171 %	2.010 %
R	1.729 %	1.713 %	1.729 %	1.713 %
$P_{\rm gas}$	2.184 %	2.037 %	2.184 %	2.037 %
$P_{\rm e}$	1.472 %	1.585 %	1.472 %	1.585 %
Quadratic Interpolation:			Quadratic Interpolation:	
$T_{\rm kin}$	0.030 %	0.032 %	0.030 %	0.032 %
$\kappa_{\rm R}$	2.702 %	2.810 %	2.702 %	2.810 %
$\tau_{\rm R}$	0.026 %	0.025 %	0.026 %	0.025 %
ρ	0.883 %	0.812 %	0.883 %	0.812 %
R	1.240 %	1.229 %	1.240 %	1.229 %
$P_{\rm gas}$	0.904 %	0.842 %	0.904 %	0.842 %
$P_{\rm e}$	0.634 %	0.677 %	0.634 %	0.677 %
Least-Square Quadratic Interpolation:			Least-Square Quadratic Interpolation:	
$T_{\rm kin}$	0.035 %	0.036 %	0.035 %	0.036 %
$\kappa_{\rm R}$	10.499 %	10.954 %	10.499 %	10.954 %
$\tau_{\rm R}$	0.033 %	0.024 %	0.033 %	0.024 %
ρ	2.905 %	2.605 %	2.905 %	2.605 %
R	3.520 %	3.489 %	3.520 %	3.489 %
$P_{\rm gas}$	2.923 %	2.645 %	2.923 %	2.645 %
$P_{\rm e}$	1.550 %	1.686 %	1.550 %	1.686 %
Cubic Spline Interpolation:			Cubic Spline Interpolation:	
$T_{\rm kin}$	0.026 %	0.027 %	0.026 %	0.027 %
$\kappa_{\rm R}$	2.439 %	2.576 %	2.439 %	2.576 %
$\tau_{\rm R}$	0.022 %	0.023 %	0.022 %	0.023 %
ρ	0.459 %	0.381 %	0.459 %	0.381 %
R	0.708 %	0.702 %	0.708 %	0.702 %
$P_{\rm gas}$	0.439 %	0.358 %	0.439 %	0.358 %
$P_{\rm e}$	0.121 %	0.089 %	0.121 %	0.089 %

Note: The tables on the left shows values where the interpolation was done over $T_{\rm eff}$ first, followed by $\log g$. The tables on the right shows values where the interpolation was done first over $\log g$. σ represents the RMS deviation over the entire atmosphere, whereas $\sigma(\tau_{\rm STD} < 1)$ is the RMS deviation computed only for values of $\tau_{\rm STD} < 1$.

while the quadratic and cubic spline methods misstimate $\kappa_{\rm R}$ by an equal magnitude, though the quadratic interpolation overestimates the exact solar values, while the cubic spline interpolation underestimates them.

Figure 2.7 shows the results of interpolating $\tau_{\rm R}(\tau_{\rm STD})$ using each of our four interpolation methods compared with calculating $\tau_{\rm R}$ from the exact solar model directly. In the upper atmosphere, quadratic and cubic spline interpolations produce nearly indistinguishable results, diverging only for $\log \tau_{\rm STD} \leq -4.5$. For $\log \tau_{\rm STD} \leq -4$, linear interpolation produces the least accurate values of $\tau_{\rm R}$, but produces the most accurate values for $-4 \leq \log \tau_{\rm STD} \leq -1$.

The most accurate interpolations are found for $T_{\rm kin}(\tau_{\rm STD})$ and $\tau_{\rm R}(\tau_{\rm STD})$. Across all interpolation methods, the displacement from the exact solar value of $T_{\rm kin}(\tau_{\rm STD})$ is found to be $\lesssim 0.05\%$, while in $\tau_{\rm R}(\tau_{\rm STD})$ it is $\lesssim 0.1\%$. The interpolations are even more accurate in the neighbourhood of $\tau_{\rm STD} \approx 2/3$, which is of great convenience since $\tau_{\rm STD} \approx \tau_{\rm R}$ at that depth for all of the above interpolation methods.

Deep in the atmosphere, at $\log \tau_{\rm STD} \gtrsim 0$, the results are significantly more difficult to interpret than those found in the upper atmosphere. With the exception of R, each quantity experiences a greater fluctuation in the relative differences, with the greatest irregularity occurring between $0 \lesssim \tau_{\rm STD} \lesssim 1$. It is in that region that the atmosphere becomes increasingly opaque. Convection begins here, the $T_{\rm kin}(\tau_{\rm R})$ relationship takes on a steeper profile, and the rate at which values change with depth increases greatly. That region is also covered by only a few layers in PHOENIX, making interpolation here very difficult.

We do not consider the least-squares quadratic interpolation method any further in this thesis, as it consistently yields the least accurate results.

2.4.4 Interpolating $\tau_{\rm R}$ or $\kappa_{\rm R}$

In the procedure described above, we calculate $\tau_{\rm R}(\tau_{\rm STD})$ for each model in our grid and interpolate to the solar parameters. Alternatively, we can interpolate $\kappa_{\rm R}(\tau_{\rm STD})$ and $R(\tau_{\rm STD})$ from our grid to

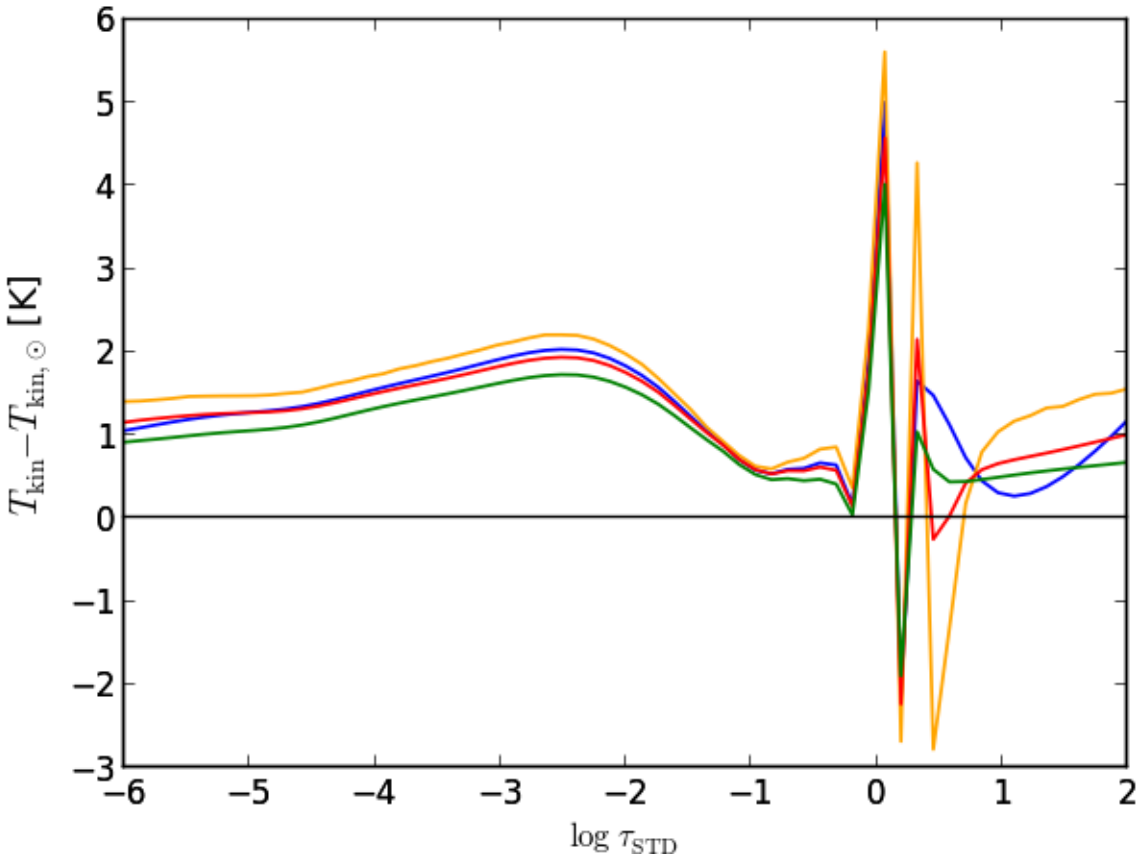

Figure 2.4: Difference between $T_{\rm kin}(\tau_{\rm STD})$ interpolated to $T_{\rm eff}$ = 5780 K, $\log g$ = 4.44 and the exact solar value. The green line represents the results of a cubic spline interpolation, the blue line linear interpolation, the red line quadratic interpolation, and the orange line is the result of the least-squares quadratic interpolation method.

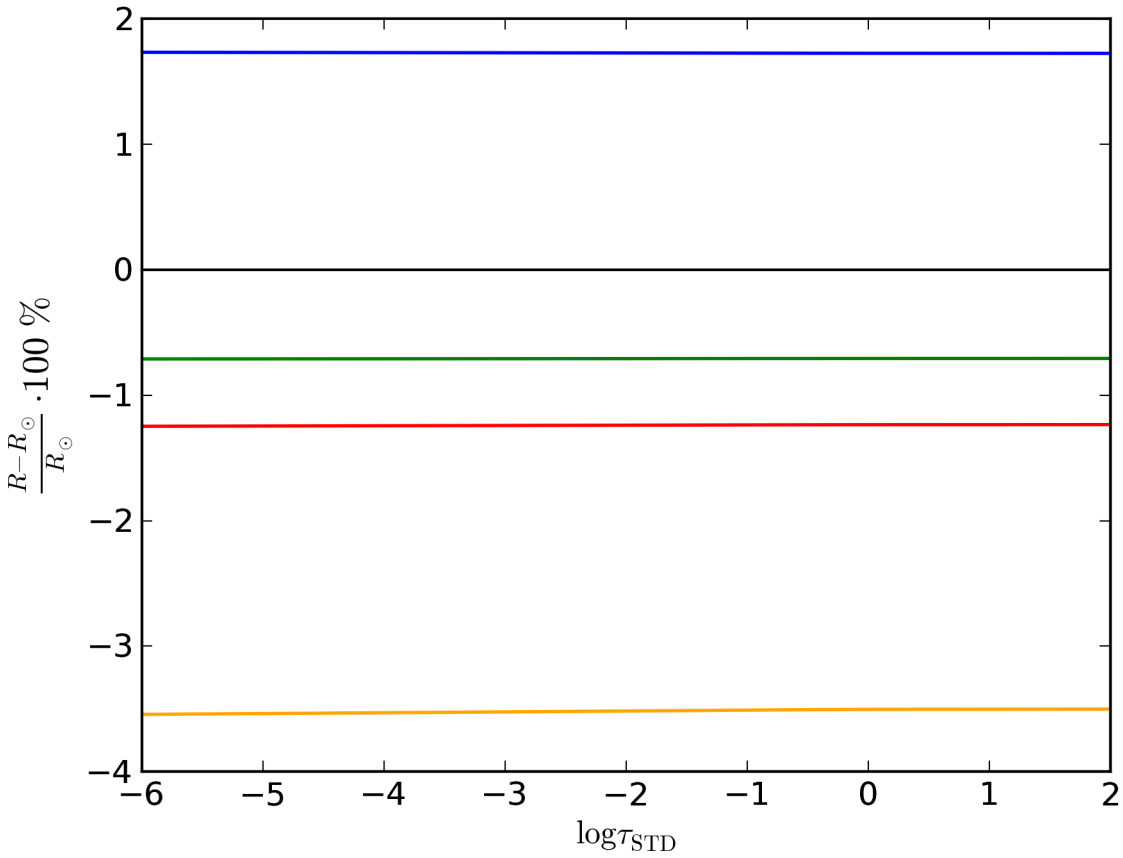

Figure 2.5: Relative difference between $R(\tau_{\mathrm{STD}})$ interpolated to T_{eff} = 5780 K, $\log g$ = 4.44 and the exact solar value. The green line represents the results of a cubic spline interpolation, the blue line a linear interpolation, the red line a quadratic interpolation, and the orange line is the least-squares quadratic interpolation method.

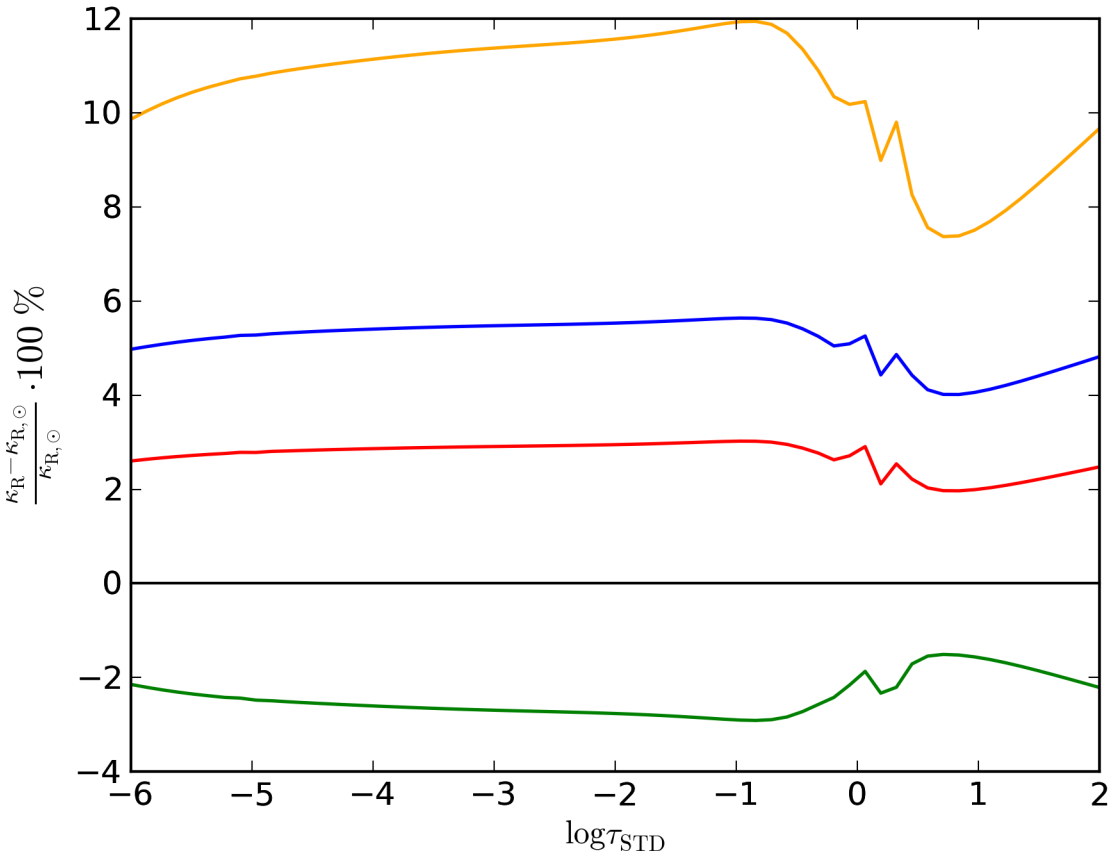

Figure 2.6: Relative difference between $\kappa_{\mathrm{R}}(\tau_{\mathrm{STD}})$ interpolated to $T_{\mathrm{eff}} = 5780$ K, $\log g = 4.44$ and the exact solar value. The green line represents the results of a cubic spline interpolation, the blue line a linear interpolation, the red line a quadratic interpolation, and the orange line is the least-squares quadratic interpolation method.

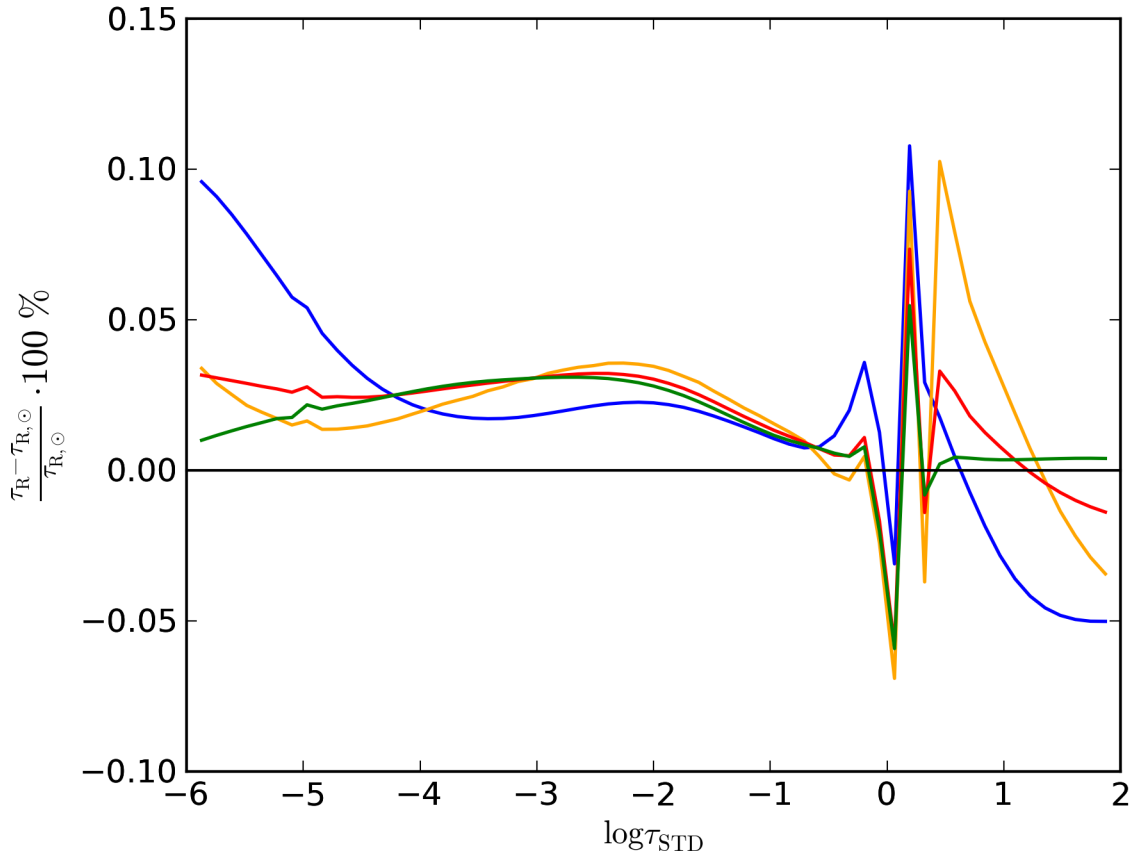

Figure 2.7: Relative difference between $\tau_{\mathrm{R}}(\tau_{\mathrm{STD}})$ interpolated to $T_{\mathrm{eff}} = 5780$ K, $\log g = 4.44$ and the exact solar value. The green line represents the results of a cubic spline interpolation, the blue line a linear interpolation, the red line a quadratic interpolation, and the orange line is the least-squares quadratic interpolation method.

the solar parameters, and calculate $\tau_{\rm R}(\tau_{\rm STD})$ from the interpolated values, $\tau_{\kappa_{\rm R}}(\tau_{\rm STD})$, using Eq. 2.19.

Figure 2.8 shows a comparison of $\tau_{\rm R}$ interpolated using each of the two procedures described here. The dashed lines show the second procedure, with $\tau_{\kappa_{\rm R}}$ calculated from interpolated values of $\kappa_{\rm R}$ and R. The figure includes solid lines, representing the direct interpolation of $\tau_{\rm R}$ from the grid of models, however the relative differences are so small compared to those of the second procedure that they are nearly indistinguishable from $\tau_{\rm R}(\tau_{\rm STD}) = \tau_{{\rm R},\odot}(\tau_{\rm STD})$. The blue lines represent linear interpolations. The red lines represent quadratic interpolations.

Because $\tau_{\kappa_{\rm R}}(\tau_{\rm STD})$ is calculated using interpolated values of $\kappa_{\rm R}(\tau_{\rm STD})$ and $R(\tau_{\rm STD})$, errors introduced into the quantities by the interpolation process are propagated to $\tau_{\kappa_{\rm R}}(\tau_{\rm STD})$ itself. As can be seen from Figures 2.5, 2.6, and 2.7, the errors in both $R(\tau_{\rm STD})$ and $\kappa_{\rm R}(\tau_{\rm STD})$ are significantly larger than the interpolation errors introduced in $\tau_{\rm R}(\tau_{\rm STD})$, and so $\tau_{\kappa_{\rm R}}(\tau_{\rm STD})$ is found to be significantly less accurate than $\tau_{\rm R}$.

2.4.5 Interpolation and grid resolution

Our grid lends itself to exploring resolutions of between 50 K and 300 K in $T_{\rm eff}$, and resolutions of between 0.5 dex to 1.5 dex in $\log g$. To accomplish that, linear interpolations were performed using the two extreme values of $\Delta T_{\rm eff}$, 50 K and 300 K, and $\Delta \log g$ = 0.5, 1.0, and 1.5 dex.

2.5 LTE *vs* NLTE solar model

LTE model atmospheres are computed utilizing the Boltzmann and Saha equations, which assume that the local kinetic temperature of the gas in the stellar atmosphere can be used to describe the distribution of electrons across the energy levels of the atoms, ions, and molecules of the stellar atmosphere. The Boltzmann equation, Eq. 2.2, gives the distribution of energy level populations of a given ionic species, and defines the excitation temperature, $T_{\rm exc}$. The Saha equation, Eq. 2.3, gives the population ratio between the ground levels of successive ionization stages of a given element,

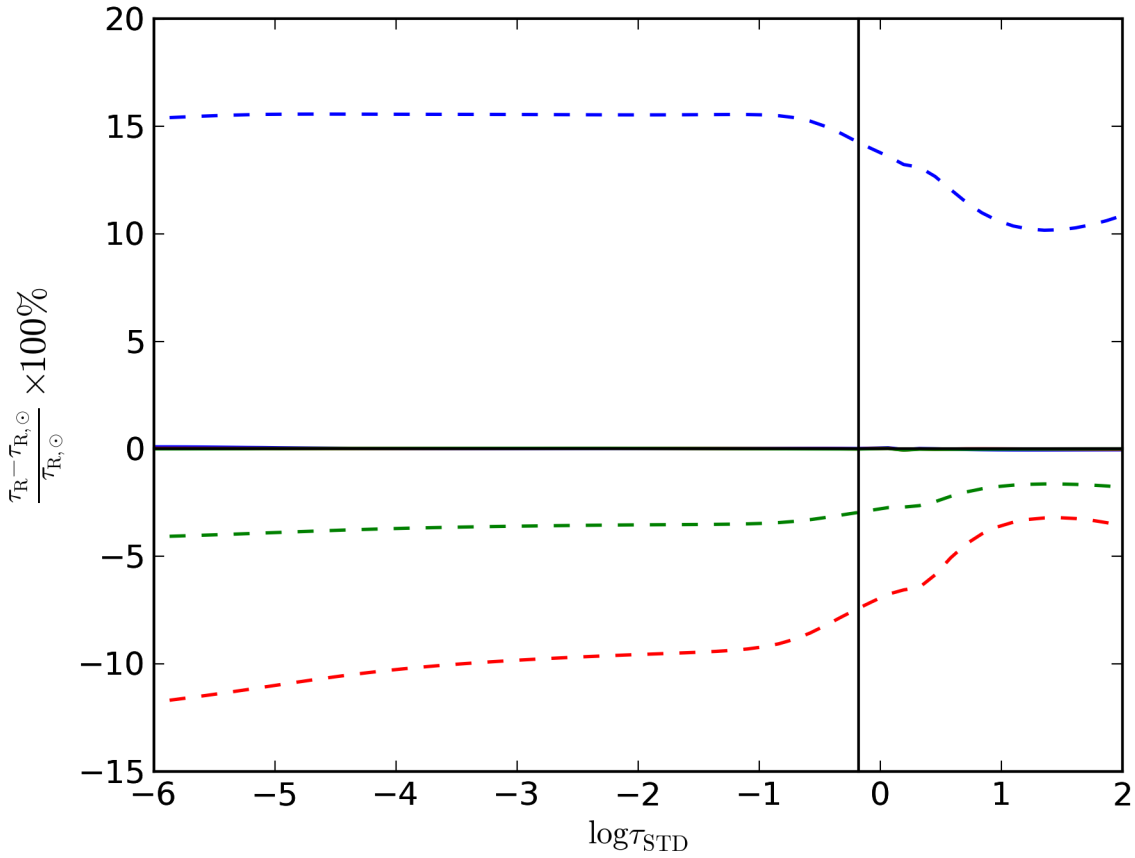

Figure 2.8: Relative differences between $\tau_{\rm R}(\tau_{\rm STD})$ as calculated using values of $\kappa_{\rm R}$ and R interpolated to the solar position of $\log g$ = 4.44, $T_{\rm eff}$ = 5780 K and the exact solar $\tau_{\rm R}(\tau_{\rm STD})$. The blue line represents a bilinear interpolation, the red line a biquadratic interpolation, and the green line a bicubic interpolation. Compare these results to those found from pre-computing the $\tau_{\rm R}$ structure of each atmosphere and interpolating $\tau_{\rm R}(\tau_{\rm STD})$ within the grid of models, as shown in Figure 2.7.

and defines the ionization temperature, $T_{\rm ion}$. In LTE, $T_{\rm ion}$ = $T_{\rm exc}$ = $T_{\rm kin}$.

NLTE model atmospheres are computed by solving the statistical equilibrium (SE) rate equation to determine the exact energy level populations of the different atomic and molecular species that compose the atmospheric gas. For a given species, the SE rate equation takes on the form

$$\begin{aligned}&\sum_{j<i} n_j(R_{ji}+C_{ji})\\&-n_i\left\{\sum_{j<i}(R_{ij}+C_{ij})+\sum_{j>i}\left(\frac{n_j^*}{n_i^*}\right)(R_{ij}+C_{ij})\right\}\\&+\sum_{j>i} n_j\left(\frac{n_j^*}{n_i^*}\right)(R_{ji}+C_{ji})=0,\end{aligned} \tag{2.21}$$

where n_i is the NLTE population and n_i^* is the LTE population of the ith energy level, (n_i^*/n_j^*) is the Saha-Boltzmann factor between levels i and j, or the continuum stage k. C_{ij} represents the collisional rates, while the radiative rates for bound-bound transitions are represented by R_{ij} and have the form

$$R_{ij} = B_{ij}\int_0^\infty \phi_{ij}(\lambda)J(\lambda)d\lambda \tag{2.22}$$

and

$$R_{ji} = A_{ji} + B_{ji}\int_0^\infty \phi_{ij}(\lambda)J(\lambda)d\lambda. \tag{2.23}$$

Here, A_{ji}, B_{ji}, and B_{ij} are the Einstein coefficients for the transitions $i \rightarrow j$, and $\phi_{ij}(\lambda)$ is the normalized line profile function for the given transition. For bound-free transitions, the radiative rates are given by

$$R_{ik} = \frac{4\pi}{hc}\int_0^\infty \sigma_{ik}(\lambda)J(\lambda)\lambda d\lambda \tag{2.24}$$

and

$$R_{ki} = \frac{4\pi}{hc}\left(\frac{n_k^*}{n_i^*}\right)\int_0^\infty \sigma_{ik}(\lambda)\lambda\left[\frac{2hc^2}{\lambda^5}+J(\lambda)\right]e^{\left(-\frac{hc}{k_{\rm B}\lambda T}\right)}d\lambda, \tag{2.25}$$

where $\sigma_{ik}(\lambda)$ is the cross-section for photo-ionization from the ith level to the continuum state k.

For solar-type stars, LTE model atmospheres have been found to closely reproduce observed fluxes for wavelengths longer than about 2700 Å. Allende Prieto et al. (2003) found $\sigma_{\rm RMS}$ between the predicted LTE and observed solar flux to be 13%, leading them to suggest that uncertainties in the atomic line data fully account for the differences between calculated and observed fluxes. They found that departures from LTE were important at shorter wavelengths where the metal ionization becomes dominant and leads to a sharp increase in opacities. Unlike PHOENIX NLTE models which consistently calculate both the structure of the atmosphere and the population levels of different species in NLTE, the models of Allende Prieto et al. (2003) were not internally consistent; rather than solving for the atmospheric structure parameters (kinetic temperature, electron pressure, and gas pressure) in NLTE, they solved the so-called restricted NLTE problem, wherein they adopted a fixed atmospheric structure calculated using the assumption of LTE, and solved the SE equations for species of interest.

Mashonkina et al. (2007) also solved the restricted NLTE problem in their study of Ca I and Ca II abundances in late-type stars and found that NLTE line fits were in good agreement, within 0.04 dex, between solar Ca I and Ca II abundances, and removed the discrepancy between the two found under the assumption of LTE.

To test the impact that the assumption of LTE has on our $T_{\rm kin}(\tau_{\rm R})$ relationships, a NLTE model atmosphere and synthetic opacity spectrum was created using the exact solar parameters of $T_{\rm eff,\odot}$ = 5780 K and $\log g_{\odot}$ = 4.44. To compute NLTE model atmospheres, PHOENIX self-consistently solves the radiative transfer equation and the NLTE SE rate equations for select ionization stages of specific species and transitions using an operator splitting/accelerated lambda iteration (OS/ALI) method (Hauschildt et al., 1999). OS/ALI takes advantage of an established operator formalism for the radiative transfer and statistical equilibrium equations and numerical approximations based on those of Cannon (1973) to solve the equations quickly using an iterative approach. The OS/ALI method is fast enough to allow many atomic ionization species to be treated in NLTE.

PHOENIX treats the lowest six ionization stages of 20 of the most important elements in NLTE, including Fe, and at least the lowest two ionization stages of 4 additional elements (Short et al.,

1999). The species used in computing our NLTE solar model, as well as the number of energy levels and bound-bound transitions included in the SE rate equations for each species, are shown in Table 2.3. As performed in Short & Hauschildt (2005), only levels connected by primary transitions (that is, transitions of $\log gf$ value greater than -3) are included in the SE rate equations. All other transitions for that species, collectively called secondary transitions, are calculated under the assumption that the occupation numbers are equal to the Boltzmann distribution value. The excitation temperatures for secondary transitions are set equal to the local value of $T_{\rm kin}$ multiplied by the NLTE ground-state departure coefficient for the next higher ionization stage. Only ionization stages that are non-negligibly populated in the Sun's atmosphere are treated in NLTE, and as a result only the first two ionization stages are included for most elements.

2.6 Data management

The calculation of $\kappa_{\rm R}$ from κ_λ presented issues with data management not present in most model stellar atmosphere or synethetic stellar spectrum computations. Because of the λ range and resolution of the opacity spectra, and because κ_λ is computed in double precision for 14 different types of physical processes, $\kappa_{\lambda,{\rm p}}$, at each of the 64 depth layers over which PHOENIX samples the atmosphere, the storage of $\kappa_{\lambda,{\rm p}}$ for each LTE atmosphere consumes a large amount of computer disc space. As can be seen from Table 2.1, each synthetic spectrum computed under LTE in our grid contains 890,112 wavelength points, resulting in 797,541,223 unique values of $\kappa_{\lambda,{\rm p}}$. Each value of $\kappa_{\lambda,{\rm p}}$ printed to disc consumes 10 bytes of storage space, resulting in each model atmosphere and synthetic spectrum in our grid occupying approximately 8 gigabytes (GB) of disc space. That resulted in our grid of 39 models, which includes models computed with $T_{\rm eff}$ = 5780 K and those computed with $\log g$ = 4.44, consuming approximately 300 GB of disc space. To save disc space we compress PHOENIX's output using the file compression and archiving utility *gzip*, resulting in a 90% compression rate for our data. Our archived grid therefore consumes approximately 28 GB of disc space.

Files cannot be read directly by our $\tau_{\rm R}$ calculator, as the contents of the files are necessarily compressed. To read $\kappa_{\lambda,{\rm p}}$ from the files, they must first be decompressed. Our $\tau_{\rm R}$ calculator has been written to call *gzip* in its decompression mode to decompress the archived data automatically before reading them. Once the data have been successfully read, the gzip utility is called one more time in its compression mode to re-compress them. That allows $\kappa_{\rm R}$ and $\tau_{\rm R}$ to be computed from our archived grid of models and spectra without the need of direct user supervision, and facilitates the use of our $\tau_{\rm R}$ calculator on resource managed high performance computing clusters.

When calculating $\kappa_{\rm R}$, we are interested only in the total κ_λ at each wavelength sampled, not the extinction resulting from each of the 14 physical processes modelled by PHOENIX, $\kappa_{\lambda,{\rm p}}$. That allows us to sum over $\kappa_{\lambda,{\rm p}}$ on the fly, as $\kappa_\lambda = \sum_{\rm p} \kappa_{\lambda,{\rm p}}$, reducing the memory requirement of our calculator from approximately 8 GB to less than 600 MB. That further facilitates the use of our $\tau_{\rm R}$ calculator on resource managed clusters.

Table 2.3: Species Treated in Non-Local Thermodynamic Equilibrium (NLTE) in the NLTE Solar Model.

	Ionization Stage		
Element	I	II	III
H	80/3160	...	...
He	19/37	...	...
Li	57/333	55/124	...
C	228/1387	...	...
N	252/2313	...	...
O	36/66	...	...
Ne	26/37	...	...
Na	53/142	35/171	...
Mg	273/835	72/340	...
Al	111/250	188/1674	...
Si	329/1871	93/436	...
P	229/903	89/760	...
S	146/439	84/444	...
K	73/210	22/66	...
Ca	194/1029	87/455	150/1661
Ti	395/5279	204/2399	...
Mn	316/3096	546/7767	...
Fe	494/6903	617/13675	...
Co	316/4428	255/2725	...
Ni	153/1690	429/7445	...

Note: Each ionization stage is labeled in the form N/L,where N represents the number of energy levels and L the number of b-b transitions included in the SE rate equations for each model atom. This table shows only those species used in the creation of our NLTE solar model. PHOENIX is capable of treating many more species in NLTE.

Chapter 3

Results

This chapter presents the results of our interpolations within the grid of stellar models. In much of the analysis, we compare the result of interpolating a function within the grid to the solar values of $T_{\rm eff}$ and $\log g$ to the same function from the solar model computed by PHOENIX, which we call the "exact" function, and which is consistently used as the baseline for the comparison.

3.1 Grid Resolution

Figure 3.1 shows a comparison of the solar temperature profile, $T_{\rm kin}(\tau_{\rm STD})$, derived by interpolating temperature profiles within our grid to the solar values of $T_{\rm eff}$ = 5780 K and $\log g$ = 4.44 using different values of $\Delta T_{\rm eff}$ and $\Delta \log g$, to the exact solar temperature profile, $T_{\rm kin,\odot}(\tau_{\rm STD})$. Lines of different colour represent different resolutions of $\log g$, with blue illustrating $\Delta \log g$ = 0.5 dex, red illustrating $\Delta \log g$ = 1.0 dex, and green illustrating $\Delta \log g$ = 1.5 dex. Solid lines represent values found by interpolating over $T_{\rm eff}$ with the highest possible resolution in our grid, $\Delta T_{\rm eff}$ = 50 K, and dashed lines represent values found using the lowest possible resolution in our grid, $\Delta T_{\rm eff}$ = 300 K. At the lowest investigated resolutions, $\Delta T_{\rm eff}$ = 300 K, and $\Delta \log g$ = 1.5, we have only two data points available to interpolate within. As a result, and for the sake of consistency, linear interpolation is used in each case in Section 3.1.

In all cases, the interpolated models overestimate the temperature in the upper atmosphere from $-6 \leq \log \tau_{\rm STD} \leq -1$. The overestimation is at a minimum at $\log \tau_{\rm STD} \approx -1$ at all resolutions, where it varies from 0 % to 0.04 %, and reaches a maximum at $\log \tau_{\rm STD} \approx -2.5$, where it varies from 0.04 % to 0.13 %. There is a general trend toward an increase in the overestimation of $T_{\rm kin}$ with decreasing resolution in $\log g$, *i.e.* increasing $\Delta \log g$. Similarly, changing the resolution in $T_{\rm eff}$ implies that higher resolutions (smaller $\Delta T_{\rm eff}$) lead to marginally better results in $T_{\rm kin}$ throughout most of the atmosphere, with the maximum overestimation being lessened by approximately 0.01% for both the $\Delta \log g$ = 0.5 and 1.5 cases. The situation becomes more complicated near the top of the atmosphere at $\log \tau_{\rm STD} \lesssim -1$, where increasing the resolution in $T_{\rm eff}$ results in an increase in the overestimation of $T_{\rm kin}$ by as much as 0.05%, as seen at the top of the atmosphere for $\log g$ = 1.0. Deeper in the atmosphere, at optical depths greater than $\log \tau_{\rm STD}$ = 0, the atmosphere becomes convective and the temperature gradient changes rapidly over a small number of depth points sampled by PHOENIX. That produces a region where interpolation within grids of all resolution becomes less reliable. $\tau_{\rm R}$ = 2/3 was found to lie above the convective zone at $\log \tau_{\rm STD} = -0.3360 \pm 0.014$, and so is unaffected by the region of less reliable interpolation.

The RMS deviation of the interpolated value of $T_{\rm kin}(\tau_{\rm STD})$ from the exact $T_{\rm kin}(\tau_{\rm STD})$ throughout the atmosphere, σ_T, varies with resolution. The value of σ_T lies between extreme values of 0.030% for $\Delta T_{\rm eff} = 50$ K and $\Delta \log g = 0.5$ dex, and 0.102% for $\Delta T_{\rm eff} = 300$ K and $\Delta \log g = 1.5$ dex. If only the region of the atmosphere located above $\log \tau_{\rm STD}$ = 0 is considered, the extrema are 0.033% and 0.097%, respectively.

Figure 3.2 is similar to Figure 3.1, except it shows the relative differences in interpolated and exact $\tau_{\rm R}(\tau_{\rm STD})$ values at solar values of $T_{\rm eff}$ and $\log g$. Decreasing the resolution in $\log g$ results in an increase in the overestimation of $\tau_{\rm R}(\tau_{\rm STD})$ at all points above the convective zone, with a maximum increase of approximately 1.2 % occurring at the very top of the atmosphere. By contrast, decreasing the resolution in $T_{\rm eff}$ results in an increasing underestimation of $\tau_{\rm R}(\tau_{\rm STD})$, with $\tau_{\rm R}(\tau_{\rm STD})$ dropping by as much as 1.1 % at the very top of the atmosphere.

As with $T_{\rm kin}$, interpolated values of $\tau_{\rm R}$ are overestimated at the top of the atmosphere for

all values of $\Delta \log g$ when interpolating within the high resolution $T_{\rm eff}$ grid, with a maximum overstimation of 2.1 % occuring for $\Delta \log g$ = 1.5. The same trend does not hold for the low resolution $T_{\rm eff}$ grid, as $\tau_{\rm R}$ at the top of the atmosphere is underestimated by 0.1 % for $\Delta T_{\rm eff}$ = 300 K and $\Delta \log g$ = 0.5 dex, and 0.9 % for $\Delta T_{\rm eff}$ = 300 K and $\Delta \log g$ = 1.0 dex. In general, values of $\tau_{\rm R}$ at the top of the atmosphere computed from grids with $\Delta T_{\rm eff}$ = 300 K are approximately 1% lower than those computed from grids with $\Delta T_{\rm eff}$ = 50 K for each resolution in $\log g$.

The RMS deviation in $\tau_{\rm R}$ throughout the atmosphere, $\sigma_{\tau_{\rm R}}$, was found to vary with resolution in both $T_{\rm eff}$ and $\log g$. The extrema of $\sigma_{\tau_{\rm R}}$ were found to be 0.059% for $\Delta T_{\rm eff} = 50$ K and $\Delta \log g = 0.5$ dex, and 0.799% for $\Delta T_{\rm eff} = 50$ K and $\Delta \log g = 1.5$ dex. If only values of $\log \tau_{\rm STD} < 0$ are considered, the values are 0.062% and 0.856%, respectively.

The results from Figures 3.1 and 3.2 have been combined into $T_{\rm kin}(\tau_{\rm R})$ relationships. The relative difference between the interpolated and exact $T_{\rm kin}(\tau_{\rm R})$ relationships for the solar atmosphere is shown in Figure 3.3, with line styles and colours as used in the previous two figures. A black vertical line indicates the special value of $\tau_{\rm R}$ = 2/3. We use $T_{2/3}$ to represent the value of $T_{\rm kin}$ at that point. The absolute difference between the interpolated and exact values of $T_{2/3}$, $\Delta T_{2/3}$, and the relative difference between the values, $\delta T_{2/3}$, are of particular interest in this thesis, and are found in Table 3.1.

With the exception of $T_{\rm kin}(\tau_{\rm R})$ interpolated using $\Delta T_{\rm eff}$ = 50 K and $\Delta \log g$ = 1.5 dex, which, as a result of the large overestimation of $\tau_{\rm R}$ seen in Figure 3.2, underestimates $T_{\rm kin}$ at the very top of the atmosphere, all interpolations of $T_{\rm kin}(\tau_{\rm R})$ overestimate the value of $T_{\rm kin}$ relative to the exact solar values by, at worst, 0.13 % for all values of $\log \tau_{\rm R} < 1$ in the atmosphere.

The RMS deviation of the interpolated $T_{\rm kin}(\tau_{\rm R})$ from the exact $T_{\rm kin}(\tau_{\rm R})$ throughout the whole atmosphere, $\sigma_{T_{\rm kin}(\tau_{\rm R})}$, was found to lie between values of 0.029%, for $\Delta T_{\rm eff} = 50$ K and $\Delta \log g = 0.5$ dex, and 0.096%, for $\Delta T_{\rm eff} = 300$ K and $\Delta \log g = 1.5$ dex. When only the atmosphere located above the convection zone, *i.e.* $\tau_{\rm STD} < 0$, is taken into consideration, the respective values are 0.031% and 0.095%. Table 3.1 lists the RMS deviation of the interpolated $T_{\rm kin}(\tau_{\rm R})$ from the exact $T_{\rm kin}(\tau_{\rm R})$ above the convection zone, $\sigma_{T_{\rm kin}(\tau_{\rm R}<1)}$, for all values of $\Delta T_{\rm eff}$ and $\Delta \log g$.

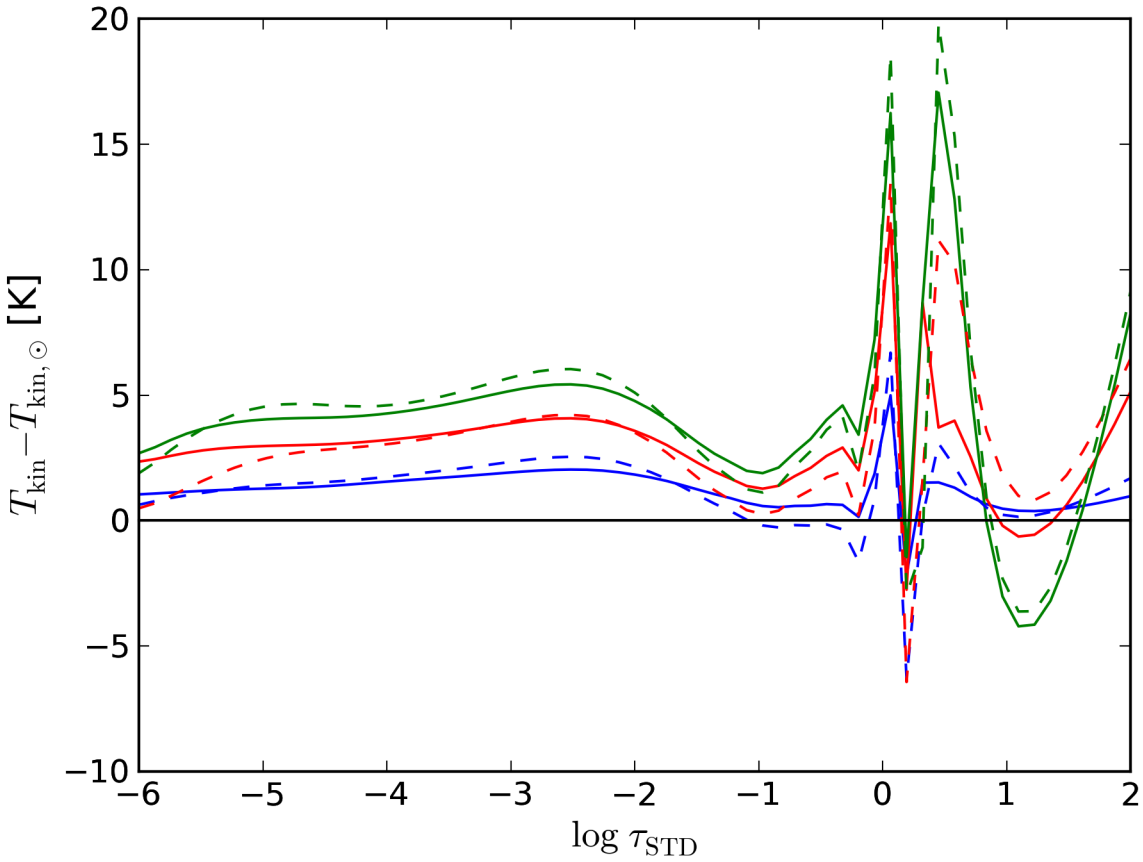

Figure 3.1: Difference between the kinetic temperature, $T_{\rm kin}(\tau_{\rm STD})$, interpolated within our model grids and the modelled solar value. Each line represents a different resolution of the grid. Solid lines show values found using $\Delta T_{\rm eff}$ = 50 K, while dashed lines show values found using $\Delta T_{\rm eff}$ = 300 K. Blue lines show the result of using $\Delta \log g$ = 0.5 dex, red lines $\Delta \log g$ = 1.0 dex, and green lines $\Delta \log g$ = 1.5 dex.

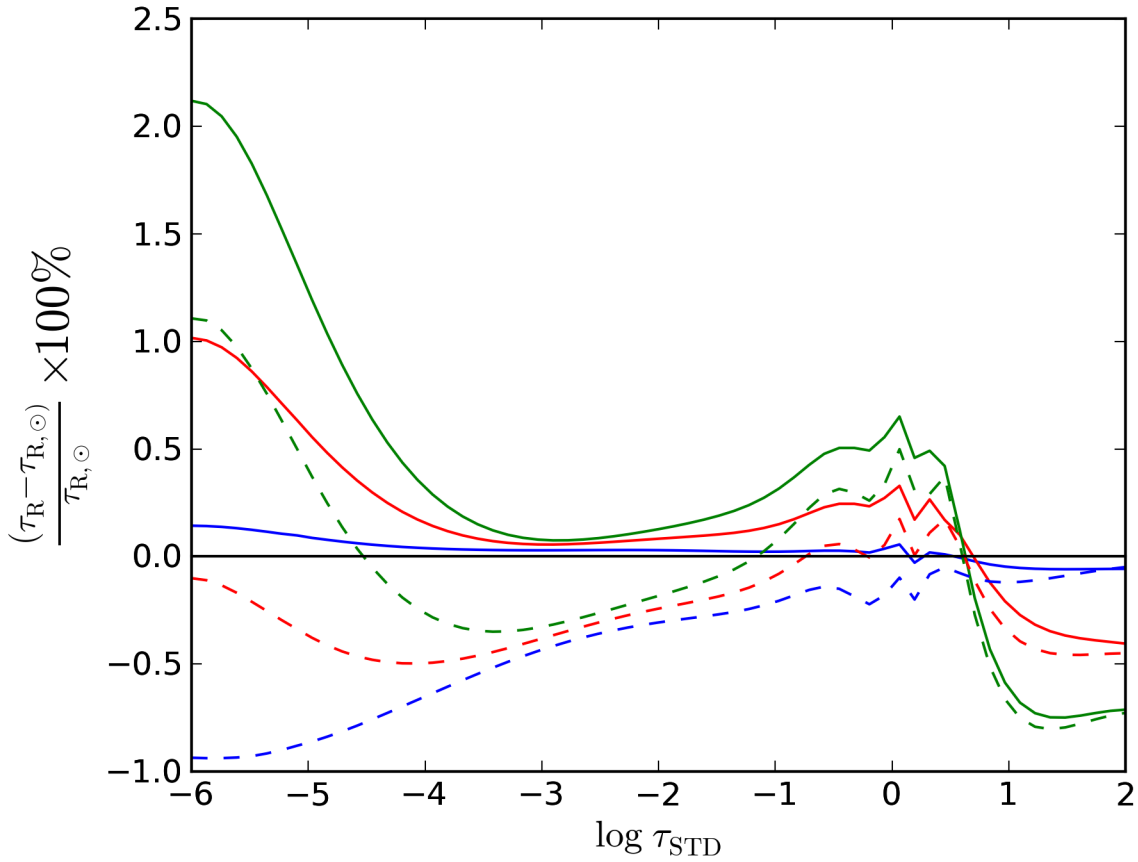

Figure 3.2: Relative difference between the Rosseland mean optical depth,$\tau_{\mathrm{R}}(\tau_{\mathrm{STD}})$, interpolated within our grid of models grids and the exact solar value. Each line is styled as described in Figure 3.1.

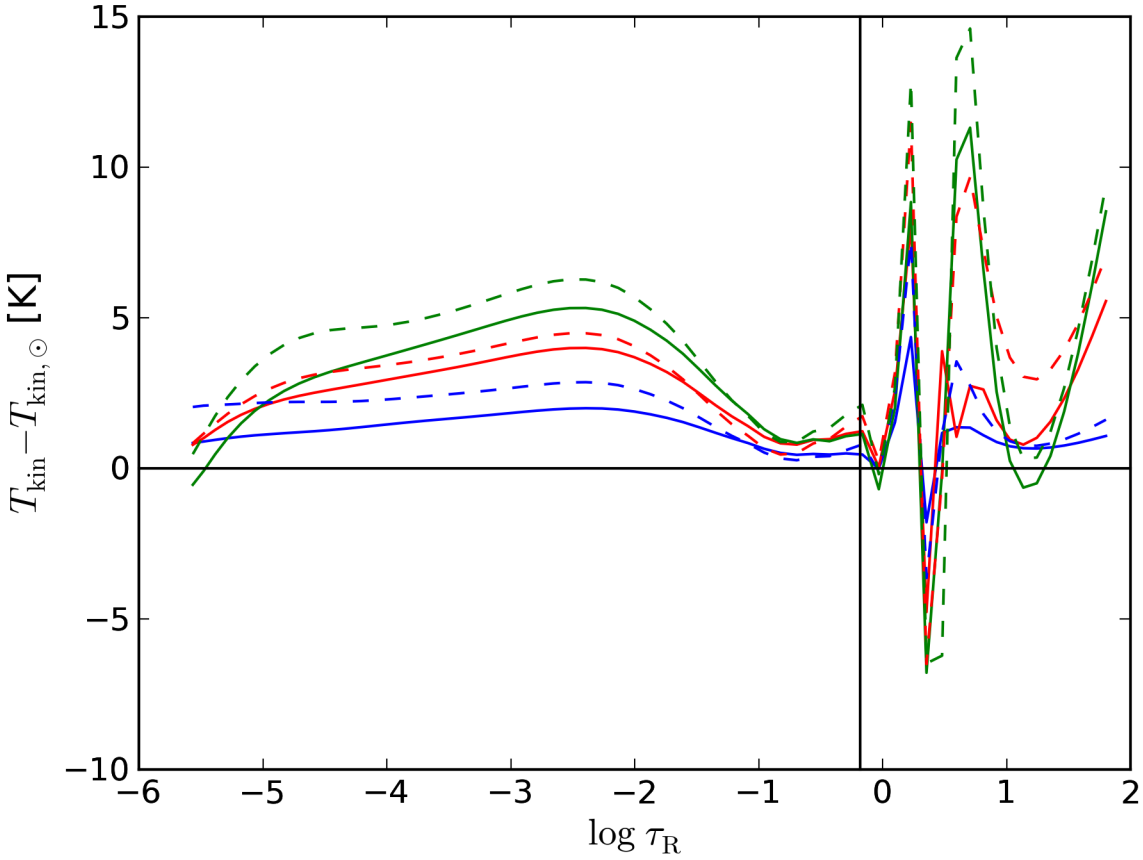

Figure 3.3: Difference between the $T_{\rm kin}(\tau_{\rm R})$ relationships interpolated within our grid of models grids and the modelled solar value. Each line is styled as described in Figure 3.1.

Table 3.1: Accuracies and Relative Differences of $T_{\rm kin}(\tau_{\rm R})$ Interpolations from our grid onto Solar Values of $T_{\rm eff}$ and $\log g$.

$\Delta T_{\rm eff}$[K]	$\Delta \log g$	$\sigma_{T_{\rm kin}(\tau_{\rm R})}$	$\sigma_{T_{\rm kin}(\tau_{\rm R}<1)}$	$\Delta T_{2/3}$ [K]	$\delta T_{2/3}$
50	0.5	0.029%	0.031%	0.47	0.008%
50	1.0	0.057%	0.060%	1.25	0.022%
50	1.5	0.076%	0.076%	1.20	0.020%
300	0.5	0.046%	0.048%	0.87	0.015%
300	1.0	0.071%	0.068%	1.70	0.029%
300	1.5	0.096%	0.095%	2.10	0.036%

Note: $\sigma_{T(\tau_{\rm R}<1)}$ represents the RMS deviation of $T_{\rm kin}$, plotted as a function of $\tau_{\rm R}$, taking into consideration the atmosphere at a height higher in the atmosphere than that which has $\tau_{\rm R}$ = 2/3, whereas $\sigma_{T_{\rm kin}(\tau_{\rm R})}$ is calculated using $T_{\rm kin}$ throughout the entire atmosphere.
$\Delta T_{2/3}$ is the absolute difference between interpolated values of $T_{\rm kin}$ at $\tau_{\rm R}$ = 2/3 and the exact solar value, whereas $\delta T_{2/3}$ represents the relative difference.

3.2 Interpolation Method

Figures 2.4 and 2.7 show the relative differences between the interpolated and exact values of $T_{\rm kin}(\tau_{\rm STD})$ and $\tau_{\rm R}(\tau_{\rm STD})$, respectively, interpolated from within our grid using four different interpolation methods at $\Delta T_{\rm eff}$ = 50 K and $\Delta \log g$ = 0.5 dex. Figure 3.4 shows the relative difference between interpolated and exact values of $T_{\rm kin}(\tau_{\rm R})$ at the same resolutions, combining the results for three of the methods. Different colours represent the different interpolation methods, with the blue curve showing the results of linear interpolation, the red curve showing the results of quadratic interpolation, and the green curve showing the results of interpolation using cubic splines.

Two-point and three-point interpolations yield comparable results, with $\sigma_{T,\rm Linear}$ = 1.48 K, or 0.030%, and $\sigma_{T,\rm Quadratic}$ = 1.44 K, or 0.030%. Interpolation by cubic splines produces more accurate results, with $\sigma_{T,\rm Cubic}$ = 1.23 K, or 0.026%. The values are 1.44 K (0.030%) and 1.40 K (0.029%) for linear and quadratic interpolations, respectively, while the results for interpolation by cubic splines remain unchanged when only the atmosphere above $\tau_{\rm R}$ = 1 is considered. $\Delta T_{2/3}$ and $\delta T_{2/3}$ resulting from linear interpolation were 0.47 K or 0.008%. Quadratic interpolation yielded differences of 0.54 K, or 0.009%, and interpolation by cubic splines resulted in values within 0.41

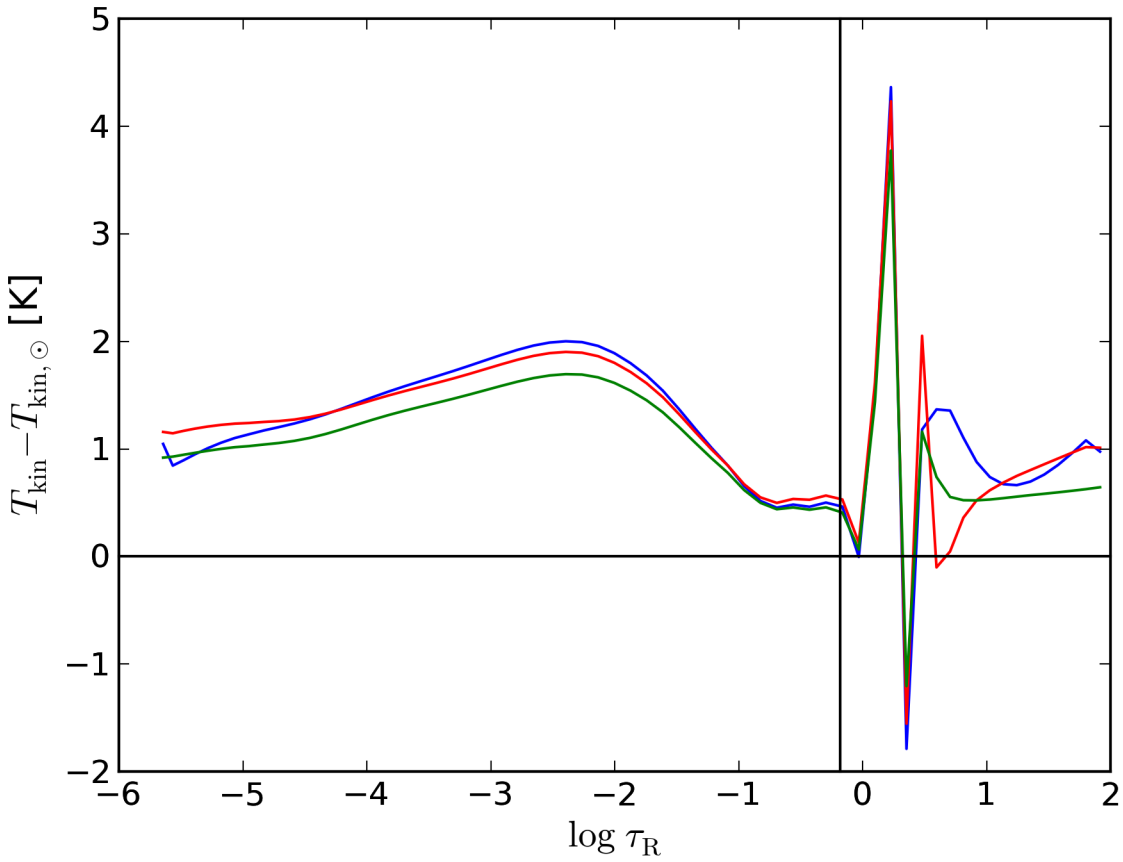

Figure 3.4: Difference between the kinetic temperature, $T_{\rm kin}$ interpolated within our grid of models and the modelled solar value, plotted as a function of $\tau_{\rm R}$. Each line represents a different interpolation method performed within our highest resolution grid ($\Delta T_{\rm eff} = 50$ K, $\Delta \log g = 0.5$ dex). The blue line shows the result of two-point interpolation, the red line three-point interpolation, and the green line interpolation using cubic splines.

Table 3.2: Least-Square Linear Regression Fit of $T_{2/3}(T_{\rm eff})$ for Different Values of $\log g$.

$\log g$	m	b [K]	R^2	p
3.5	0.952	269	0.999991	7.8×10^{-14}
4.0	0.490	289	0.999997	5.1×10^{-15}
4.5	0.944	323	0.999998	2.5×10^{-15}
5.0	0.947	308	0.999977	8.6×10^{-13}

Note: m is the slope of the least-squares best fit line, and b is the value of $T_{2/3}$ extrapolated to $T_{\rm eff}$ = 0 K.

K, or 0.007%.

3.3 $T_{2/3}$ as a Function of $T_{\rm eff}$ and $\log g$

Figure 3.5 plots $T_{\rm kin}$ at $\tau_{\rm R}$ = 2/3 for different values of $\log g$ plotted as a function of $T_{\rm eff}$. The blue line represents $\log g$ = 3.5, the red line $\log g$ = 4.0, the green line $\log g$ = 4.5, and the orange line $\log g$ = 5.0. The relationship between $T_{\rm eff}$ and $T_{2/3}$ is linear for each value of $\log g$ with the coefficient of determination, R^2, reaching values greater than 0.9999, and p-values less than 8.6×10^{-13}, in all four cases. The results of a least-square linear regression performed on each line can be found in Table 3.2.

For LTE atmospheric models, the grey approximation to the radiative transfer equation yields the result that $T_{2/3}$ = $T_{\rm eff}$. Our results deviate from such a situation slightly, because PHOENIX does not produce grey atmospheres, as can be seen from Table 3.2 and Figure 3.5. The line $T_{2/3}$ = $T_{\rm eff}$ with slope $m = 1$ and $T_{2/3}$ intercept of 0 K is shown as a dashed black line. Deviations from the $T_{2/3}$ = $T_{\rm eff}$ line for all values of $\log g$ are shown in Figure 3.6. The deviations are also shown to be highly linear within the $T_{\rm eff}$ range of our grid, with $R^2 > 0.99$ and $p < 1.6 \times 10^{-6}$ for all values of $\log g$. Detailed results of the least-squares linear regression for the deviation of $T_{2/3}$ from $T_{\rm eff}$ as a function of $T_{\rm eff}$ are found in Table 3.3.

As all explored values of $\log g$ resulted in slopes of $T_{2/3}(T_{\rm eff}) < 1$ and extrapolated $T_{2/3}$ intercepts > 0 K, each line of constant $\log g$ will have some critical value of $T_{\rm eff}$ such that

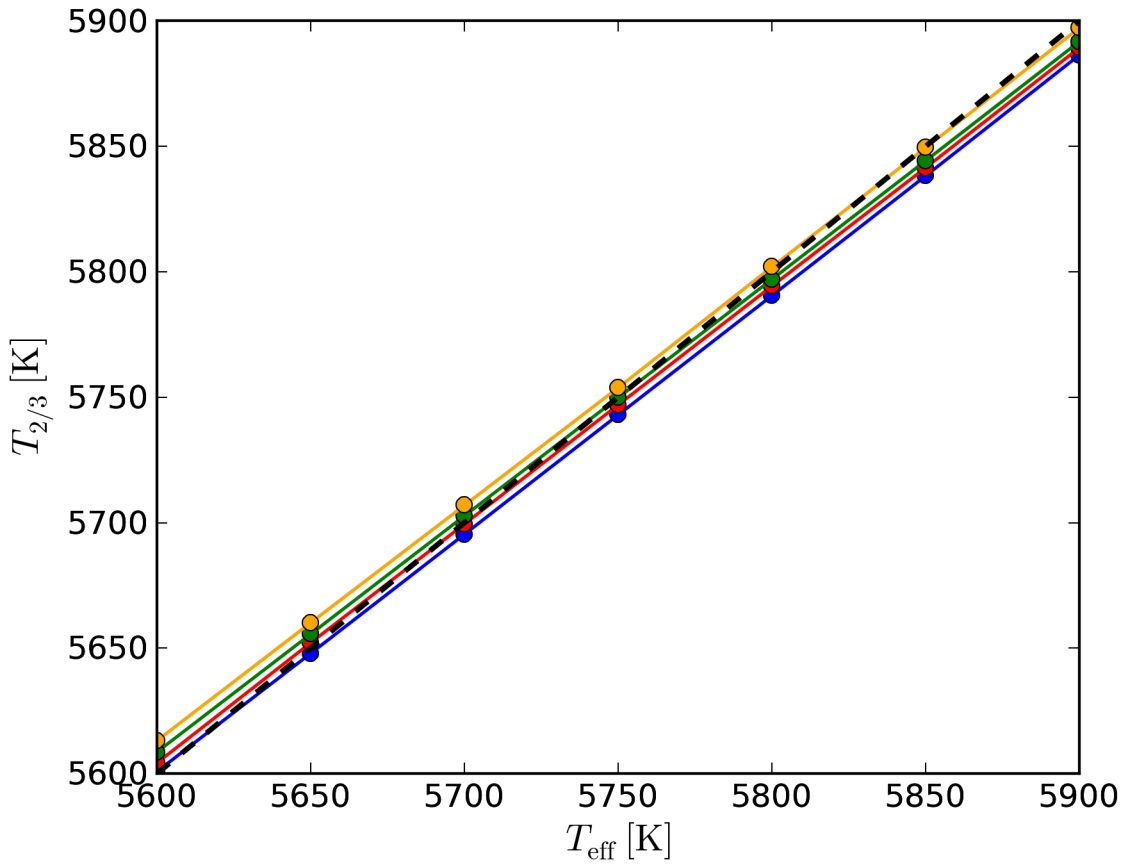

Figure 3.5: $T_{2/3}$ throughout out grid as a function of $T_{\rm eff}$. The lines are best fits. Blue shows $T_{2/3}(T_{\rm eff})$ for $\log g = 3.5$; red shows $\log g = 4.0$; green shows $\log g = 4.5$; and orange shows $\log g = 5.0$. The dashed black line represents $T_{2/3} = T_{\rm eff}$.

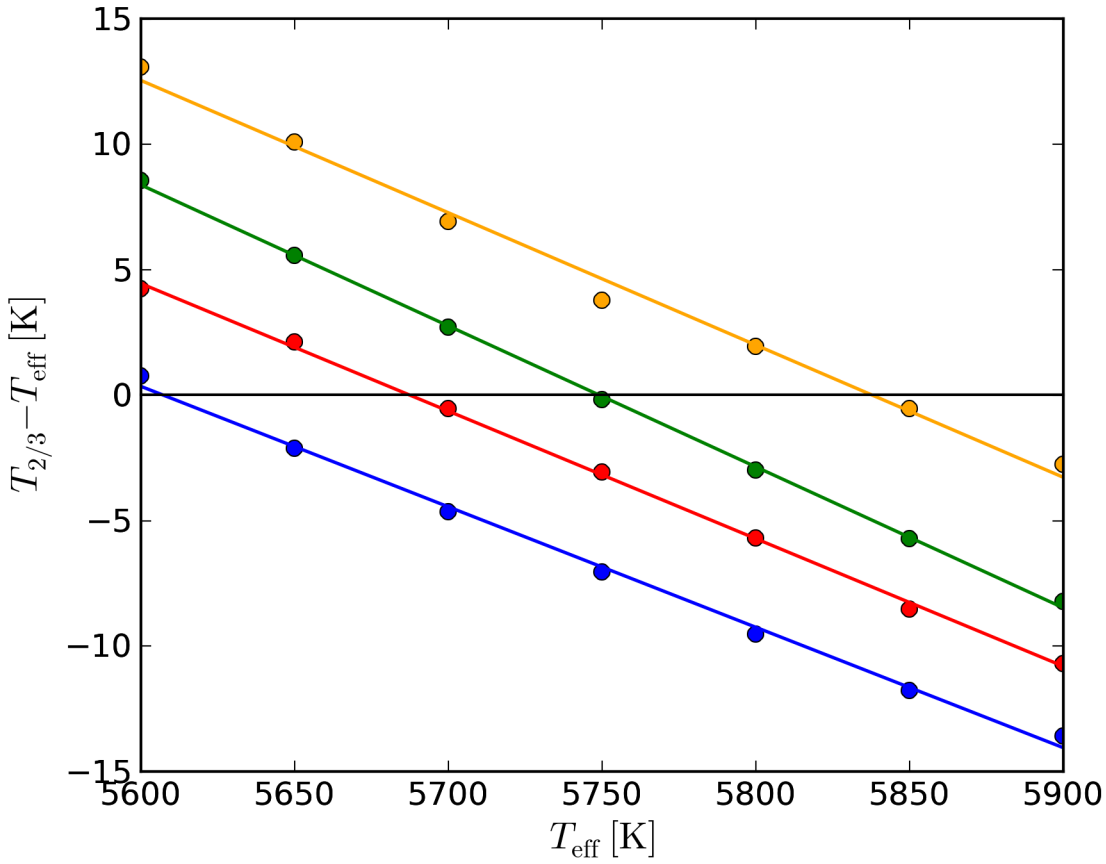

Figure 3.6: The differences between $T_{2/3}$ and $T_{\rm eff}$ for each value of $\log g$. The lines are best fits and are coloured as in Fig. 3.5.

Table 3.3: Least-Square Linear Regression Fit of $T_{2/3} - T_{\rm eff}$ vs $T_{\rm eff}$ for Different Values of $\log g$.

$\log g$	m	b [K]	R^2	p
3.5	-0.048	269	0.996547	2.4×10^{-7}
4.0	-0.051	289	0.998971	1.2×10^{-8}
4.5	-0.056	323	0.999376	303×10^{-9}
5.0	-0.053	308	0.992626	1.6×10^{-6}

Note: m is the slope of the least-squares best fit line, and b is the value of $T_{2/3} - T_{\rm eff}$ extrapolated to $T_{\rm eff}$ = 0 K.

Table 3.4: Values of $T_{\rm eff}$ where $T_{2/3}$ = $T_{\rm eff}$ for Different Values of $\log g$.

$\log g$	$T_{\rm eff}$ [K]
3.5	5613
4.0	5688
4.5	5746
5.0	5838

$T_{2/3} = T_{\rm eff}$. Below that value of $T_{\rm eff}$, $T_{2/3} > T_{\rm eff}$, and above it $T_{2/3} < T_{\rm eff}$. The critical values are represented in Figure 3.6 by the intercepts of each line with $T_{2/3} - T_{\rm eff} = 0$ K, and are listed in Table 3.4.

3.4 LTE *vs* NLTE Atmospheres

Figure 3.7 shows the $T_{\rm kin}(\tau_{\rm R})$ relationships for the LTE solar model, illustrated in blue, and the NLTE solar model, shown in red. The vertical black line highlights the value of $\tau_{\rm R}$ = 2/3. Line-blanketed atmospheres exhibit a well-known phenomenon known as backwarming, wherein spectral absorption lines block a fraction of the outgoing radiative flux, trapping it deeper in the atmosphere, and leading to an increase in temperature. Near the surface of line-blanked atmospheres, where the gas density is low enough for the atmosphere to become optically thin, regions of the spectrum that are opaque at greater depths in the atmosphere become transparent, leading to an increase in the probability of photon escape. That allows the atmosphere to maintain

radiative equilibrium at a lower temperature than would be possible in the absence of absorption lines (Carbon, 1979). Of particular importance in solar-type stars are lines resulting from absorption by Fe I, which dominate a large part of the spectrum.

In LTE model atmospheres, absorption line strengths are calculated using Boltzmann-Saha statistics, which depend only on the *local* kinetic temperature of the gas. Non-LTE calculations account for deviations from the Boltzmann, Saha, and Planck distributions caused by non-local radiation transfer. In particular, NLTE calculations account for the effect of an excess of ultraviolet radiation, relative to LTE, with an origin deep in the atmosphere where the radiation temperature, $T_{\rm Rad}$, is higher than the local kinetic temperature of the gas, $T_{\rm kin}$. That ultraviolet excess shifts the ionization equilibrium of Fe I/Fe II further toward Fe II, resulting in an increase in the rate of ionization of Fe I when compared to LTE (Athay & Lites, 1972), an effect known as NLTE overionization. Because of the large number of Fe I lines found in the spectrum of solar-type stars, such a reduction in the amount of Fe I in the atmosphere leads to a dramatic decrease in the strength of the Fe I lines. That results in a net decrease in the opacity of the atmosphere in the line forming regions, since the amount of Fe II in the solar atmosphere is large relative to the amount of Fe I, and the impact of the additional Fe II produced by the increased ionization of Fe I on the strength of the Fe II lines is negligible.

PHOENIX does not compute $T_{\rm kin}(\tau_{\rm R})$ directly, so we have found $T_{\rm kin}(\tau_{\rm STD})$ and $\tau_{\rm R}(\tau_{\rm STD})$ for both the LTE and NLTE models of the solar atmosphere and combined the results to produce our $T_{\rm kin}(\tau_{\rm R})$ relationships. Figure 3.8 shows the relative difference in $\tau_{\rm R}(\tau_{\rm STD})$ between the NLTE model, shown in red, and the LTE model. The NLTE model predicts higher values of $\tau_{\rm R}$ throughout the entire atmosphere relative to the LTE model, with the difference peaking at approximately 47% at the top of the atmosphere, and falling to a minimum of approximately 11% at $\tau_{\rm STD} \approx 2.1$. For the NLTE model, $\tau_{\rm R}$ = 2/3 at $\log \tau_{\rm STD} = -0.40$, while the same value of $\tau_{\rm R}$ was found at $\log \tau_{\rm STD} = -0.34$ in the LTE model.

The relative difference between $\kappa_{\rm R}(\tau_{\rm STD})$ in the NLTE and LTE exact solar models, shown in red in Figure 3.9, follows a similar trend to that of $\tau_{\rm R}(\tau_{\rm STD})$. The NLTE model predicts larger values

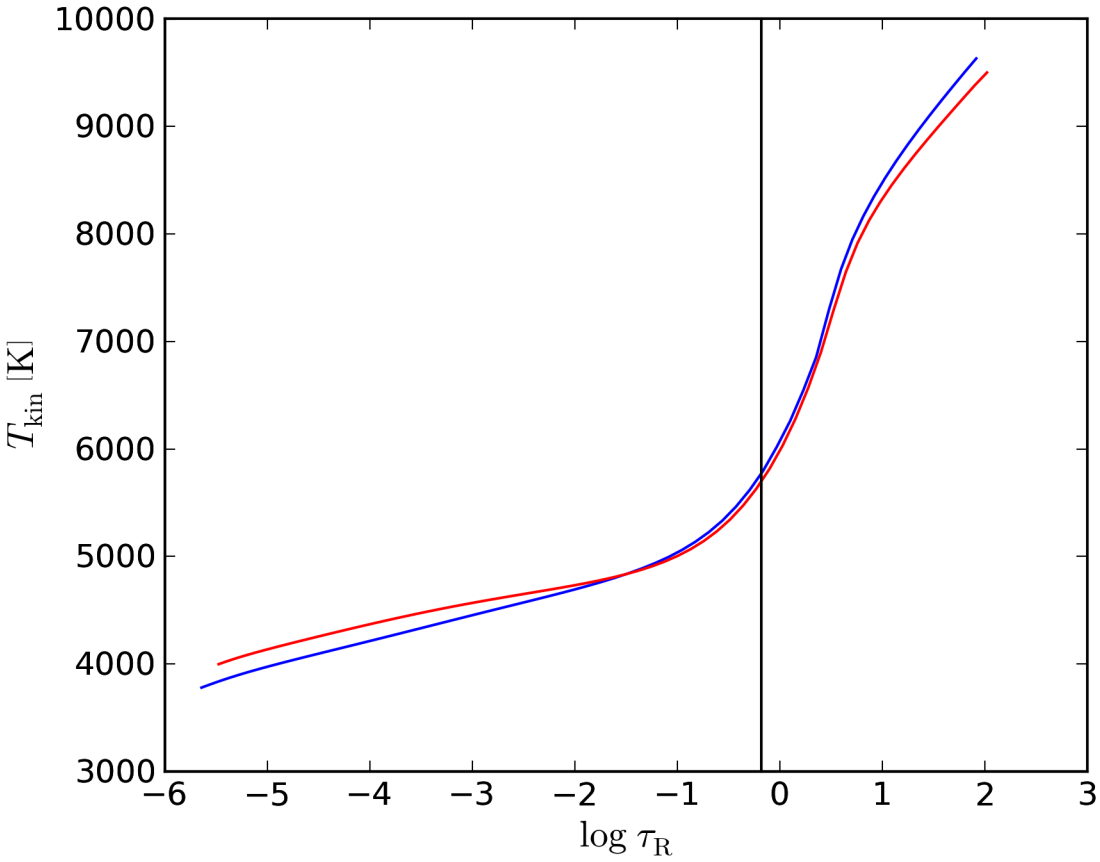

Figure 3.7: $T_{\rm kin}(\tau_{\rm R})$ relationships for LTE and NLTE models of the Sun. The blue line shows the relationship computed under the assumption of LTE. The red line shows the NLTE relationship.

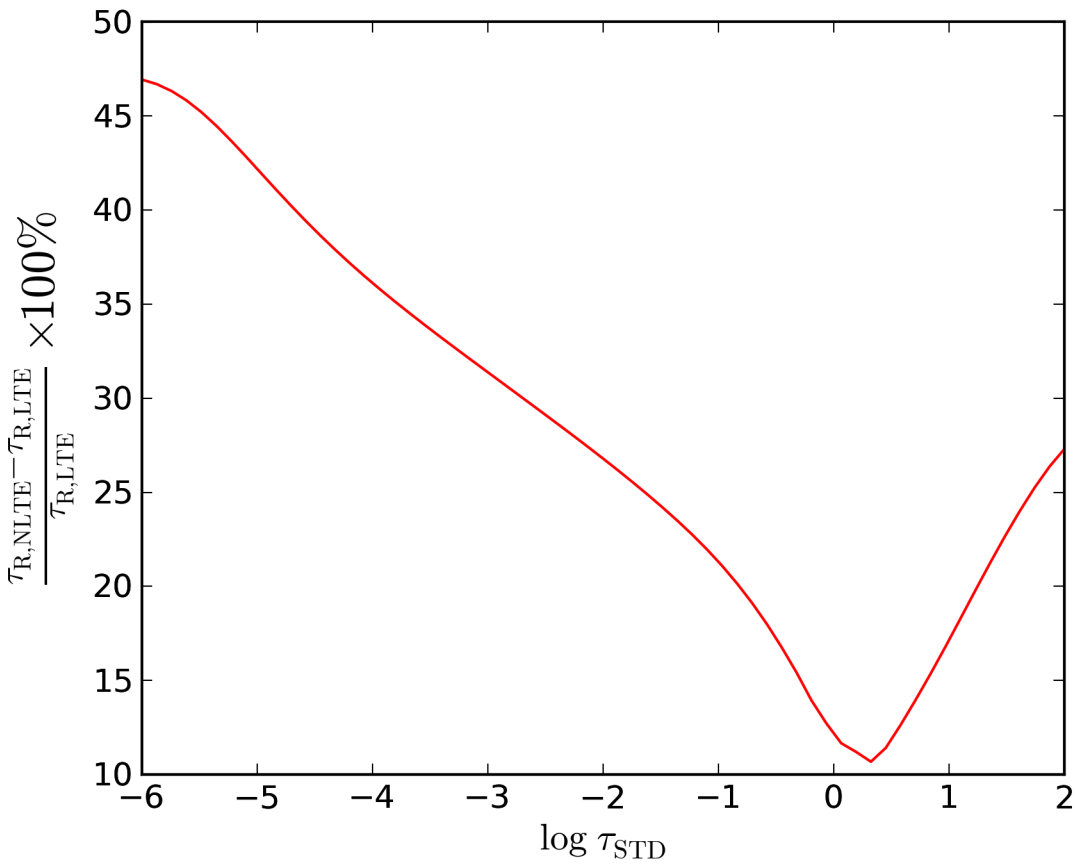

Figure 3.8: Relative difference in τ_{R} for the comparison of the NLTE solar model to the LTE solar model.

of $\kappa_{\rm R}$ at all values of $\tau_{\rm STD}$, with the maximum relative difference of 42% occurring at the very top of the atmosphere, and the minimum relative difference of 9% occurring at $\tau_{\rm STD} \approx 2.1$. The global increase in $\kappa_{\rm R}$ is caused in part by the extra electrons liberated by Fe I overionization binding with neutral hydrogen atoms, H I, leading to an increase in the $\rm H^-$ component of the continuous opacity.

Surface values of the gas density, ρ, were found to be approximately 4.5% lower in the NLTE model compared with those in the LTE model, as seen in Figure 3.10, and only exceed LTE values at depths greater than $\log \tau_{\rm STD} = -3.67$. The NLTE solar model underestimates the geometric radius of the Sun, R, by between 0.0005% and 0.0042% compared with the LTE model, as seen in Figure 3.11. $\rm dR$ is found to be negative for $0 \leq \tau_{\rm STD} \leq 0.006$ and $2.1 \leq \tau_{\rm STD} \leq 100$. Neither the differences in ρ nor those in R between the LTE and NLTE models are significant enough to drive the increase of $\tau_{\rm R}(\tau_{\rm STD})$ in the NLTE model shown in Figure 3.8.

The cause of the global increase in values of $\kappa_{\rm R}(\tau_{\rm STD})$, and thus the increased values of $\tau_{\rm R}(\tau_{\rm STD})$, in the NLTE model is found in differences in κ_λ between the LTE and NLTE model. Figure 3.12 shows a running box-car mean of $\kappa_\lambda(\lambda)$ for both the LTE solar model, shown in red, and the NLTE solar model, shown in green, at an optical depth of $\log \tau_{\rm STD} = -0.32$, the nearest value of $\tau_{\rm STD}$ sampled by PHOENIX to $\tau_{\rm R}(\tau_{\rm STD}) = 2/3$ for both models. The running mean was performed with a box-car width of approximately 1000 Å for the sake of visual clarity. The mean value of κ_λ over the whole atmosphere was found to be $4.9 \times 10^{-5}{\rm cm}^{-1}$ in the LTE model, and $14.4 \times 10^{-5}{\rm cm}^{-1}$, or 2.9 times higher, in the NLTE model.

Figure 3.13 shows the relative difference in $T_{\rm kin}(\tau_{\rm STD})$ between the NLTE and LTE model atmospheres. The NLTE model predicts larger values of $T_{\rm kin}$ everywhere above the convective region of the atmosphere ($\tau_{\rm STD} < 1$), with temperatures exceeding those predicted by the LTE model by approximately 5.76% at the top of the atmosphere. The NLTE results approach the LTE results in the region $-1 \leq \log \tau_{\rm STD} \leq 0$, which is the range in which we find $\tau_{\rm R}$ = 2/3 for both models.

The relative difference in the $T_{\rm kin}(\tau_{\rm R})$ relationships between the NLTE and LTE models is shown in Figure 3.14. The reduced efficiency of the backwarming and surface cooling effects in the

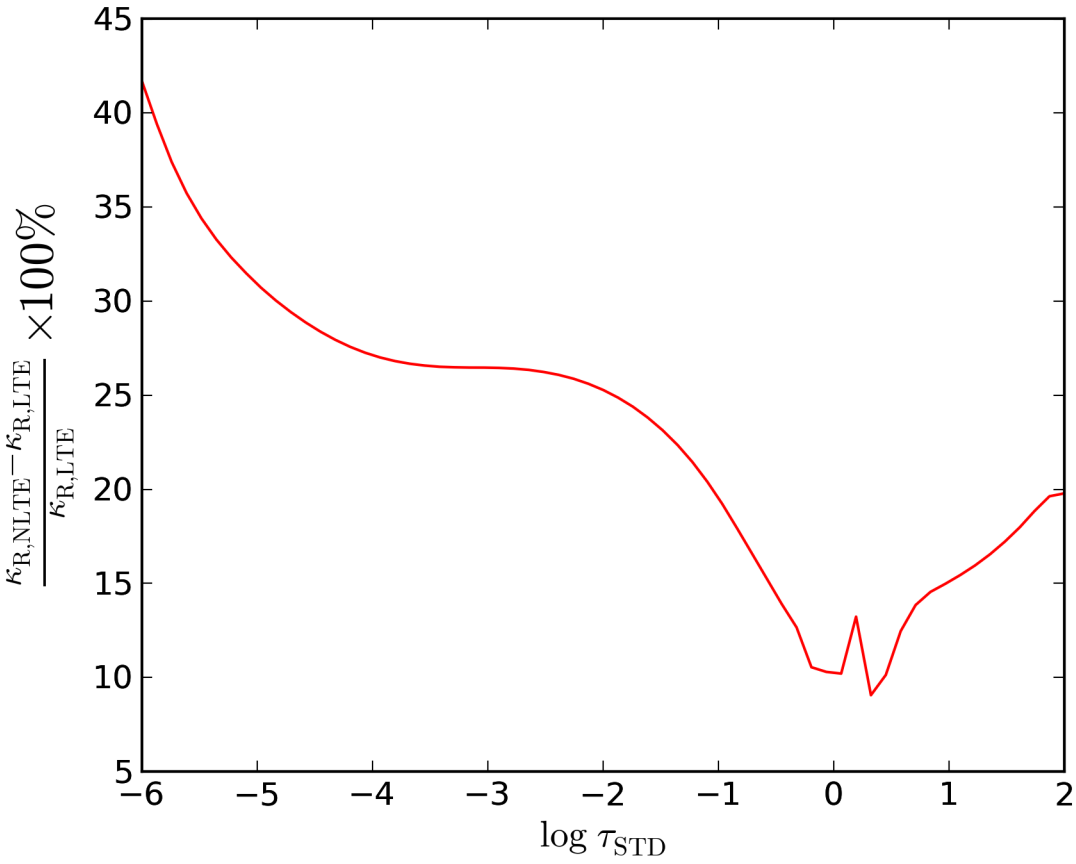

Figure 3.9: Relative difference in κ_{R} for the comparison of the NLTE solar model to the LTE solar model.

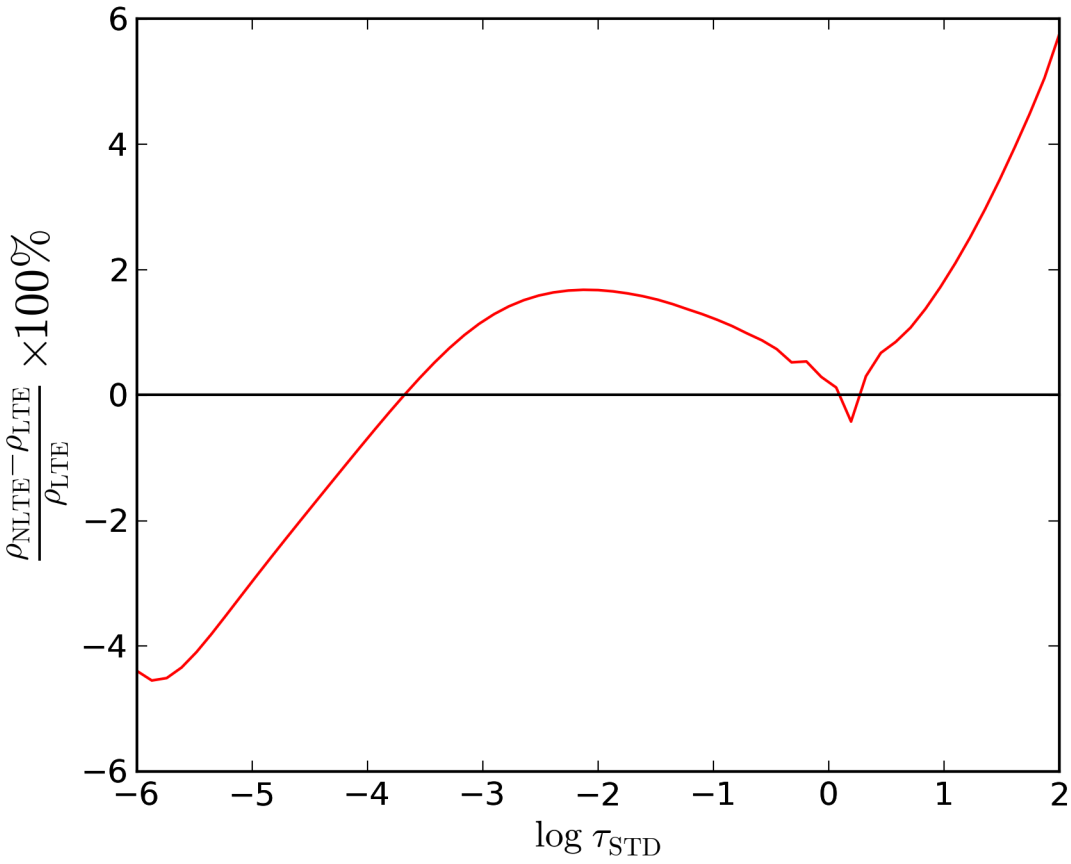

Figure 3.10: Relative difference in gas density, ρ, for the comparison of the NLTE solar model to the LTE solar model.

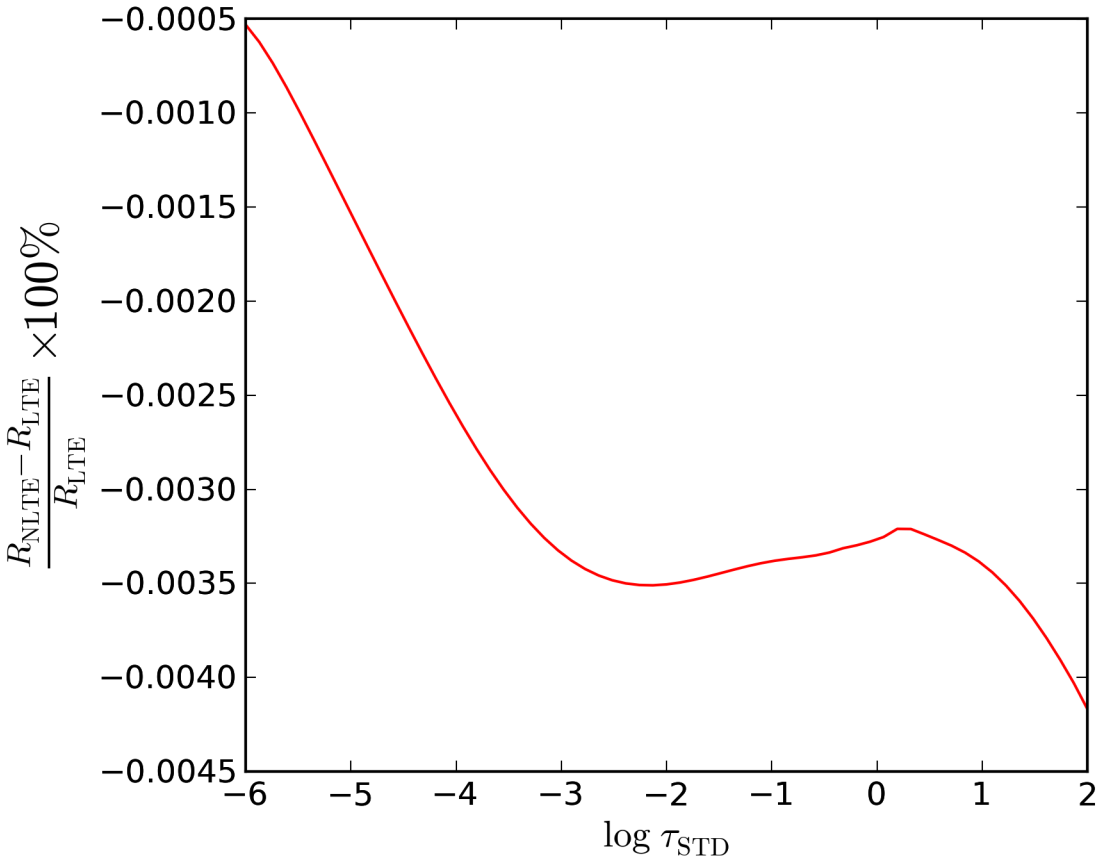

Figure 3.11: Relative difference in solar radius, R, for the comparison of the NLTE solar model to the LTE solar model.

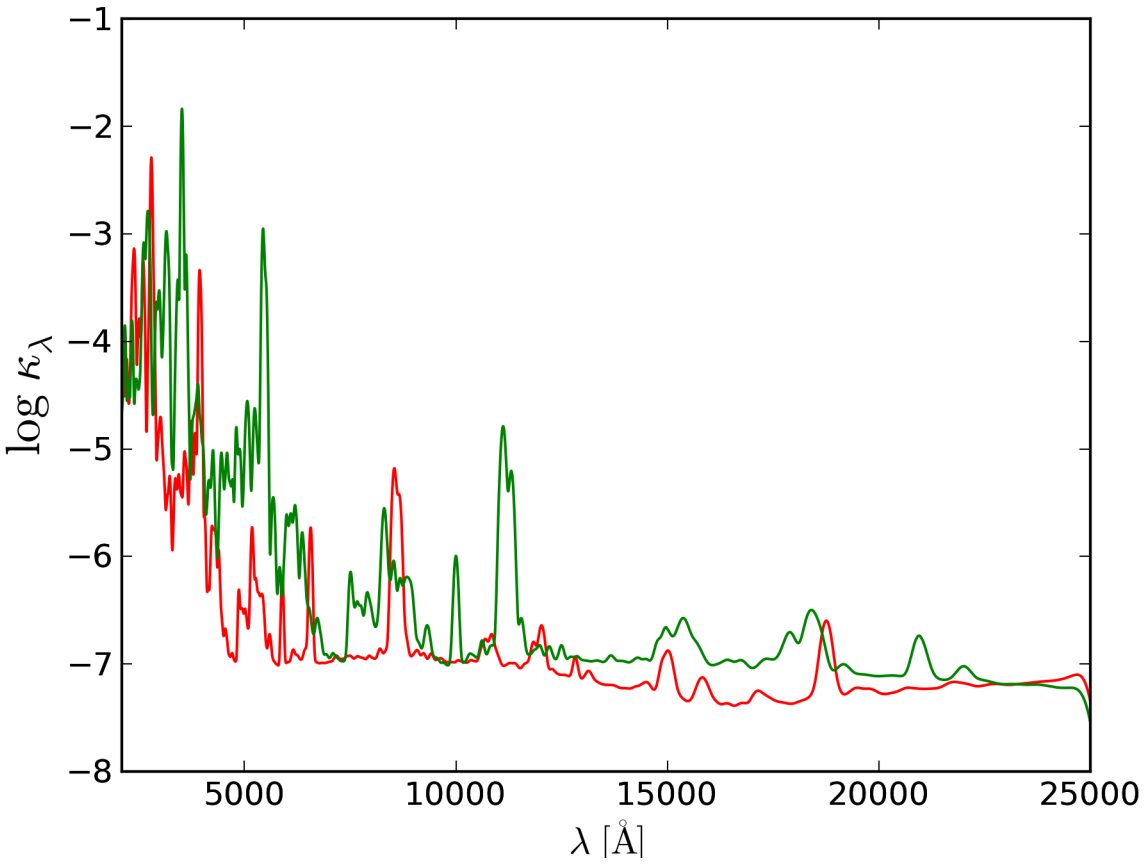

Figure 3.12: κ_λ spectrum for LTE and NLTE exact Solar models at $\tau_{\mathrm{R}} \approx 2/3$. The red line shows the LTE spectrum, while the green line is the NLTE spectrum.

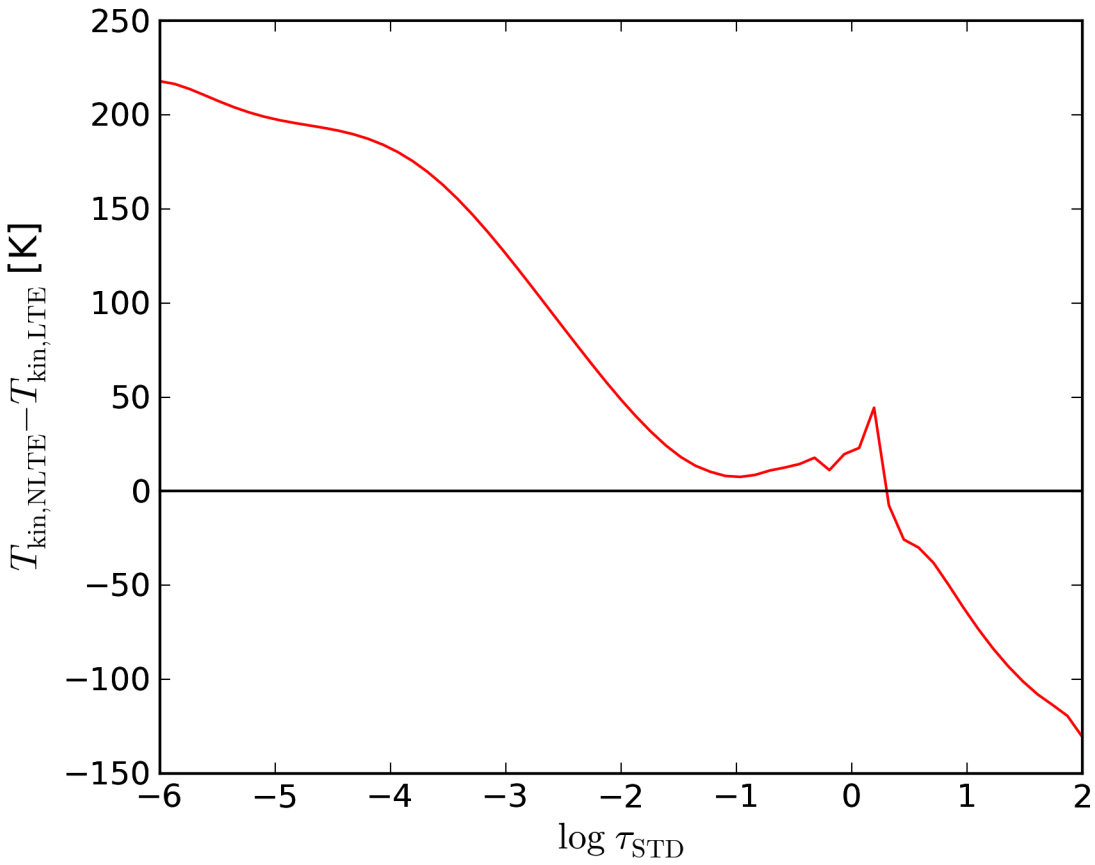

Figure 3.13: Difference in $T_{\mathrm{kin}}(\tau_{\mathrm{STD}})$ between the NLTE solar model and the LTE solar model.

NLTE model compared with those for the LTE model are clearly seen. $T_{\rm kin}$ at $\tau_{\rm R}$ = 2/3, represented by the interception of the curve with the vertical black line, is 1.25%, or 73.27 K, cooler in the NLTE model than it is in the LTE model.

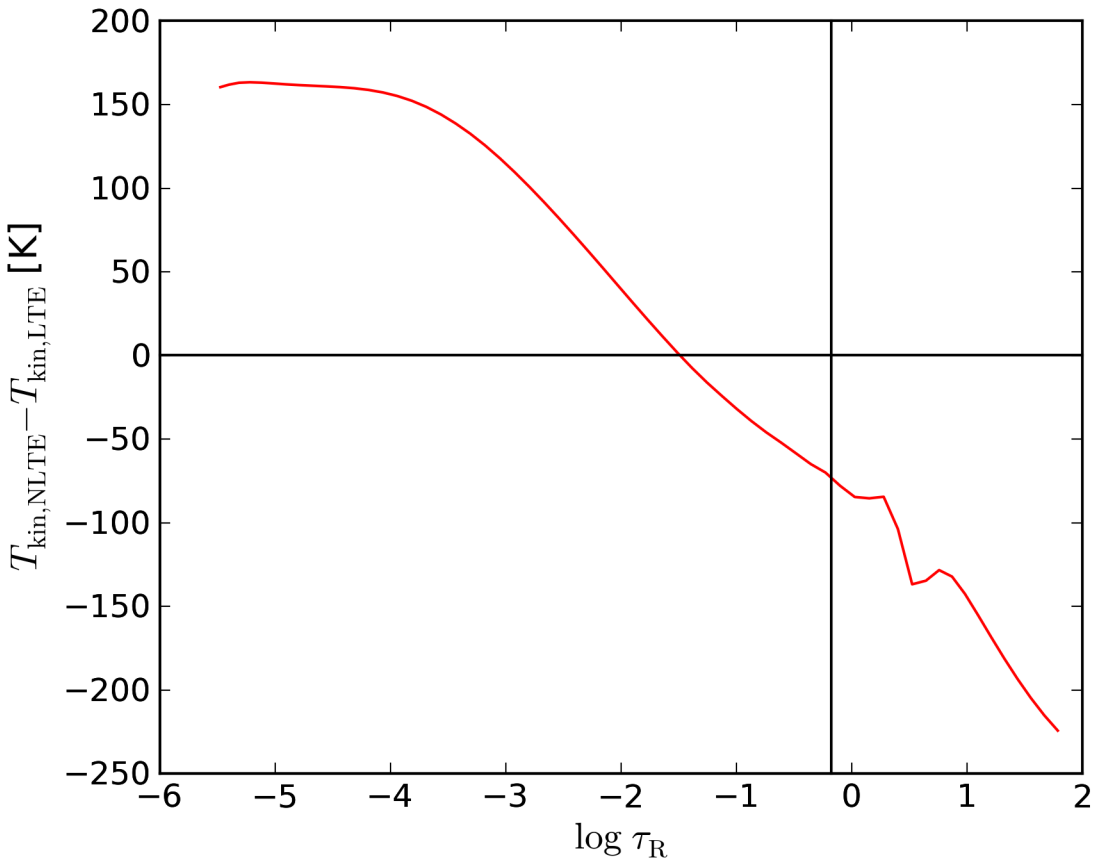

Figure 3.14: Difference in $T_{\mathrm{kin}}(\tau_{\mathrm{R}})$ between the NLTE Solar Model and the LTE Solar Model.

Chapter 4

Conclusions

In this thesis we have investigated the accuracy of four different methods for interpolating the structure of stellar atmospheres from a grid of precomputed near-solar spherical LTE model atmospheres. In particular we have tested the accuracy of the interpolations of the $T_{\rm kin}(\tau_{\rm R})$ relationship for use as the outer boundary condition in on-demand calculations of stellar structure and asteroseismological modelling at arbitrary $T_{\rm eff}$ and $\log g$. By interpolating $T_{\rm eff}$ and $\tau_{\rm R}$ within our grid of models to solar values of $T_{\rm eff}$ and $\log g$ and comparing the resulting $T_{\rm kin}(\tau_{\rm R})$ relation against that of an exact model of the Sun, we find comparable RMS deviations in $T_{\rm kin}$, taken over the whole atmosphere, for both linear and quadratic interpolations, while interpolation by cubic splines produces marginally better results. For almost every other structural parameter, interpolation by cubic splines generated improved results over the linear and quadratic methods, with deviations in ρ, R, and $P_{\rm gas}$ being smaller by a factor of 2 and the deviation in $P_{\rm e}$ being smaller by a factor of 7, compared with results from quadratic interpolation. Least-squares quadratic interpolation resulted in a deviation in $T_{\rm kin}$ that was marginally larger than the linear or quadratic methods, however it produced deviations in R and $\kappa_{\rm R}$ that were larger by a factor of approximately 3 and 4, respectively. Differences in $T_{\rm kin}$ at $\tau_{\rm R}$ = 2/3 between the interpolated and exact solar models were found to be similar for linear, quadratic, and cubic spline interpolations.

The sensitivity of linear interpolations to the resolution of our grid in both $T_{\rm eff}$ and $\log g$ and to the order in which the interpolations are performed (along $T_{\rm eff}$ then $\log g$, or *vice versa*), were also tested. Decreasing the grid spacing in $T_{\rm eff}$ from 300 K to 50 K decreased both the RMS deviation in $T_{\rm kin}$ throughout the atmosphere and the difference in $T_{\rm kin}$ at $\tau_{\rm R}$ = 2/3 by a factor of approximately 1.5, while decreasing the grid spacing in $\log g$ from 1.5 dex to 0.5 dex decreased the same values by a factor of 2.

Over the investigated range of $T_{\rm eff}$ the value of $T_{2/3}(T_{\rm eff})$ was found to vary linearly for each value of $\log g$ investigated, with deviations from a grey atmosphere also found to be linear over the range of our grid.

We calculated a NLTE solar model and found that it predicts higher values of the kinetic temperature for the atmosphere relative to the LTE model for values of $\log \tau_{\rm R} \lesssim -1.5$, with a maximum overestimation of approximately 4% at the top of the atmosphere, while it underestimated the kinetic temperature for values of $\log \tau_{\rm R} \gtrsim -1.5$. The reduction in the effects of backwarming and surface cooling is a known NLTE effect, caused in part by the weakening of Fe I absorption lines through overionization by UV radiation deep within the atmosphere reaching the line forming regions, something not accounted for under LTE, resulting in $T_{\rm kin}$ at $\tau_{\rm R}$ = 2/3 approximately 73 K cooler than in the LTE solar model.

4.1 Future Work

The results presented with this thesis have been prepared with the hope that they will be of use as upper boundary conditions in stellar structure and asteroseismology models. With the methods of Gruberbauer et al. (2012), it will be possible to test the accuracy of our $T_{\rm kin}(\tau_{\rm R})$ relationships for the outer boundary condition using a probabilistic approach.

Given the limited range over which we have developed our grid, we are looking to expand our LTE calculations to smaller values in both $T_{\rm eff}$ and $\log g$ in order to encompass the red giant branch. Our goal is to map the variability in $T_{\rm eff}$ at $\tau_{\rm R}$ = 2/3 for G-type and later stars. Doing so will

also open the door to explore further the impact of the resolution of our grid on the accuracy of interpolations within our grid of models by allowing us to study grids with $\Delta T_{\rm eff} > 300K$ and $\Delta \log g > 1.5$ dex. Moreover, given the large differences between our LTE and NLTE solar models, we hope to develop a NLTE grid of models in parallel with our LTE grid so that we can establish the variability in $T_{\rm eff}$ at $\tau_{\rm R}$ = 2/3 for NLTE atmospheres.

Bibliography

Allende Prieto, C., Hubeny, I., & Lambert, D. L. 2003, ApJ, 591, 1192

Asplund, M., Grevesse, N., & Sauval, A. J. 2005, in Astronomical Society of the Pacific Conference Series, Vol. 336, Cosmic Abundances as Records of Stellar Evolution and Nucleosynthesis, ed. T. G. Barnes, III & F. N. Bash, 25

Asplund, M., Grevesse, N., Sauval, A. J., & Scott, P. 2009, ARA&A, 47, 481

Athay, R. G., & Lites, B. W. 1972, ApJ, 176, 809

Aufdenberg, J. P., Hauschildt, P. H., Shore, S. N., & Baron, E. 1998, ApJ, 498, 837

Barbier, D. 1946, Annales d'Astrophysique, 9, 173

Cannon, C. J. 1973, J. Quant. Spec. Radiat. Transf., 13, 627

Carbon, D. F. 1979, ARA&A, 17, 513

Christensen-Dalsgaard, J., & Thompson, M. J. 1997, MNRAS, 284, 527

Christensen-Dalsgaard, J., Dappen, W., Ajukov, S. V., et al. 1996, Science, 272, 1286

Claverie, A., Isaak, G. R., McLeod, C. P., van der Raay, H. B., & Cortes, T. R. 1979, Nature, 282, 591

Demarque, P., Guenther, D. B., Li, L. H., Mazumdar, A., & Straka, C. W. 2008, Ap&SS, 316, 31

Deubner, F.-L. 1975, A&A, 44, 371

Duvall, Jr., T. L., & Harvey, J. W. 1983, Nature, 302, 24

Grevesse, N., & Sauval, A. J. 1998, Space Sci. Rev., 85, 161

Gruberbauer, M., & Guenther, D. B. 2013, MNRAS, 432, 417

Gruberbauer, M., Guenther, D. B., & Kallinger, T. 2012, ApJ, 749, 109

Guenther, D. B., Demarque, P., Kim, Y.-C., & Pinsonneault, M. H. 1992, ApJ, 387, 372

Gustafsson, B., Edvardsson, B., Eriksson, K., et al. 2008, A&A, 486, 951

Hauschildt, P. H., Allard, F., & Baron, E. 1999, ApJ, 512, 377

Kjeldsen, H., Bedding, T. R., & Christensen-Dalsgaard, J. 2008, ApJ, 683, L175

Krishna Swamy, K. S. 1966, ApJ, 145, 174

Kurucz, R., et al. 1991, NATO ASI Series, Kluwer, Dordrecht, 441

Leibacher, J. W., & Stein, R. F. 1971, Astrophys. Lett., 7, 191

Leighton, R. B., Noyes, R. W., & Simon, G. W. 1962, ApJ, 135, 474

Li, L. H., Robinson, F. J., Demarque, P., Sofia, S., & Guenther, D. B. 2002, ApJ, 567, 1192

Mashonkina, L., Korn, A. J., & Przybilla, N. 2007, A&A, 461, 261

Montalbán, J., Kupka, F., D Antona, F., & Schmidt, W. 2001, A&A, 370, 982

Morel, P., van't Veer, C., Provost, J., et al. 1994, A&A, 286, 91

Rudkjobing, M. H. 1947, On the atmospheres of the B-stars.

Short, C. I., & Hauschildt, P. H. 2003, ApJ, 596, 501

—. 2005, ApJ, 618, 926

Short, C. I., Hauschildt, P. H., & Baron, E. 1999, ApJ, 525, 375

Ströemgren, B., Gyldenkaerne, K., Rudkjobing, M., & Thernoee, K. A. 1944, Publikationer og mindre Meddeler fra Kobenhavns Observatorium, 138, 1

Strömgren, B. 1940, On the Chemical Composition of the Solar Atmosphere, 218

Ulrich, R. K. 1970, ApJ, 162, 993

VandenBerg, D. A., Edvardsson, B., Eriksson, K., & Gustafsson, B. 2008, ApJ, 675, 746